AD-A140 773 IDENTIFICATION OF SCATTERING MECHANISMS FROM MEASURED IMPULSE RESPONSE SI..(U) OHIO STATE UNIV COLUMBUS ELECTROSCIENCE LAB W J LEEPER FEB 84 ESL-712693-1 1/1

UNCLASSIFIED N00014-78-C-0049 F/G 17/9 NL

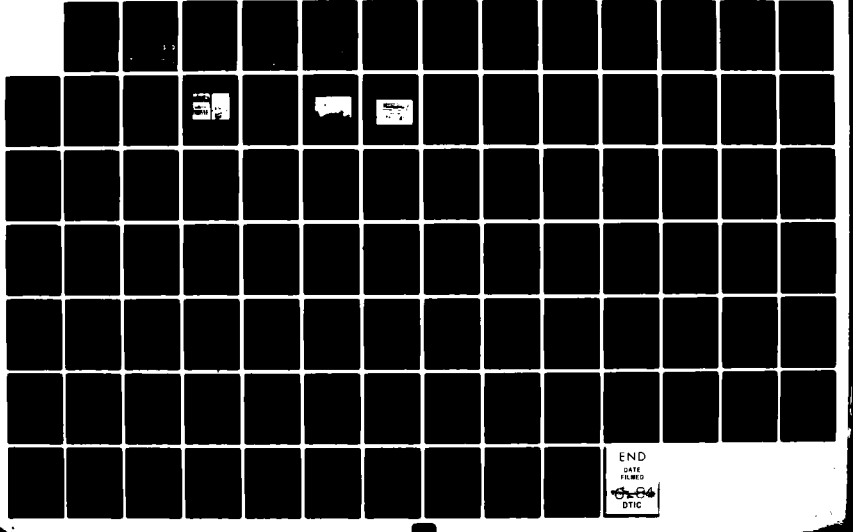

END

DATE FILMED

DTIC

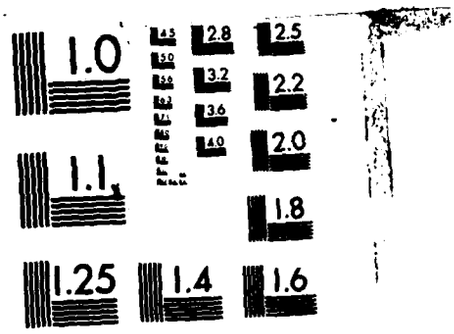

(12)

OSU

The Ohio State University

IDENTIFICATION OF SCATTERING MECHANISMS FROM MEASURED IMPULSE RESPONSE SIGNATURES OF SEVERAL CONDUCTING OBJECTS

W.J. Leeper

The Ohio State University

ElectroScience Laboratory

Department of Electrical Engineering
Columbus, Ohio 43212

Technical Report 712693-1
Contract No. N00014-78-C-0049
February 1984

NOTICES

When Government drawings, specifications, or other data are used for any purpose other than in connection with a definitely related Government procurement operation, the United States Government thereby incurs no responsibility nor any obligation whatsoever, and the fact that the Government may have formulated, furnished, or in any way supplied the said drawings, specifications, or other data, is not to be regarded by implication or otherwise as in any manner licensing the holder or any other person or corporation, or conveying any rights or permission to manufacture, use, or sell any patented invention that may in any way be related thereto.

AD-A140 773

50272-101

REPORT DOCUMENTATION PAGE	1. REPORT NO.	2.	3. Recipient's Accession No.

4. Title and Subtitle
IDENTIFICATION OF SCATTERING MECHANISMS FROM MEASURED IMPULSE RESPONSE SIGNATURES OF SEVERAL CONDUCTING OBJECTS

5. Report Date
February 1984

6.

7. Author(s)
W.J. Leeper

8. Performing Organization Rept. No.
ESL 712693-1

9. Performing Organization Name and Address
The Ohio State University ElectroScience Laboratory
Department of Electrical Engineering
Columbus, Ohio 43212

10. Project/Task/Work Unit No.

11. Contract(C) or Grant(G) No.
(C)
(G) N00014-78-C-0049

12. Sponsoring Organization Name and Address
Department of the Navy
Office of Naval Research,
Arlington, Virginia 22217

13. Type of Report & Period Covered
Technical Report

14.

15. Supplementary Notes

16. Abstract (Limit: 200 words)

The backscattered impulse response of several perfectly conducting objects has been measured and qualitatively compared to several theoretical predictions. The value of the impulse response waveform as a time history of scattering behavior is due to its unique relationship to the geometry of the scatterer. This relationship is explored for local diffraction mechanisms, multiple diffraction between separate points on the scatterer, creeping waves, and natural resonances. Finally, it is demonstrated that a time domain view of a high frequency solution such as the Uniform Geometrical Theory of Diffraction offers a physically intuitive explanation for individual scattering mechanisms and multiple interactions.

17. Document Analysis a. Descriptors

b. Identifiers/Open-Ended Terms

c. COSATI Field/Group

18. Availability Statement

DISTRIBUTION STATEMENT A
Approved for public release;
Distribution Unlimited

19. Security Class (This Report)	21. No. of Pages
Unclassified	84
20. Security Class (This Page)	22. Price
Unclassified	

(See ANSI-Z39.18) See Instructions on Reverse

OPTIONAL FORM 272 (4-77)
(Formerly NTIS-35)
Department of Commerce

TABLE OF CONTENTS

LIST OF FIGURES

CHAPTER I

INTRODUCTION

The value of the impulse response waveform as a means of characterizing a radar target was suggested by Kennaugh and Cosgriff [1] in 1958 and refined by Kennaugh [2], and Kennaugh and Moffatt [3], [4]. The impulse response is that function of time which describes the field scattered by a radar target illuminated by an impulsive plane wave. The impulse response, $F_I(t)$, and the normalized transfer function, $F(j\omega)$, of the scatterer are a Fourier transform pair. The ideal impulse response can only be approximated, whether by theory or experiment, and while such approximations show varying degrees of success, the term impulse response will be used herein to refer to the entire range of approximations.

The value of the impulse response lies mainly in its intimate relationship to the geometry of the target. The times of arrival of the contributions from individual scattering mechanisms on the target can be easily predicted on the time axis of the impulse response waveform. This relationship provides an intuitive "feel" for the scattering properties of each target geometry. The insight it affords is especially valuable when used in conjunction with high frequency scattering theories, such as the Uniform Theory of Diffraction (UTD),

which localize and superpose the contributions from individual scattering mechanisms on the target.

The early studies mentioned above used a combination of time and frequency domain techniques and low and high frequency solutions to the scattered field to assemble impulse response approximations for several simple geometries. The Rayleigh law of scattering provided a set of moment conditions on the impulse response, while physical optics predicted the high frequency behavior. The approximations were greatly improved by using the high frequency predictions of the Geometrical Theory of Diffraction. Various estimates of the impulse response waveform for several simple targets are derived in [4] and dicussed in more detail in Chapter IV.

These studies sparked an interest in coherent frequency domain backscattering measurements, since $|F(j\omega)|^2$ is related to the radar cross section of a scatterer by a multiplicative constant. A measured impulse response waveform may be obtained as the inverse Fourier transform of $F(j\omega)$ measured over a broad band of frequencies. The bandwidth requirement is the primary problem in the measurement of impulse responses. Approximations of the ramp response, the second integral of the impulse response, have been constructed from measurements at just ten harmonically related frequencies [5]. While the ramp response is valuable in such radar signature areas as target imaging [6], it will not yield the impulse response. A bandwidth of approximately 100:1 is necessary to obtain a good impulse response [6].

The present study extends the measured transfer function to a practically continuous spectrum covering a 96:1 bandwidth. Using target dimension scaling on a broadband, stepped frequency measurement system, it was possible to measure $F(j\omega)$ at frequencies beginning in the Rayleigh region, spanning the resonance region, and extending into the optics region. This is the first attempt to extend the bandwidth of the measured $F(j\omega)$ to that sufficient for the construction of an accurate approximation to the measured impulse response waveform.

One of the objectives of this study has been to assemble "complete" complex scattering cross section data for several canonical radar targets. The data are complete in the following respects:

(1) Both amplitude and phase of the backscattered signal were measured.

(2) The data cover a 96:1 bandwidth.

(3) The backscattered signal was measured for three polarizations of the transmit and receive radar: vertical-vertical, horizontal-horizontal, and vertical-horizontal.

(4) The measurements were made at look angles of every 15 degrees from 0 to 180 degrees.

(5) The vertical-horizontal (cross) polarized measurements were made at aspects out of the principal planes of the targets.

The data bank assembled from these measurements is of interest to those doing inverse scattering research, to scattering analysts, and to

those interested in the use or control of a radar target's scattering properties.

Chapter II describes the frequency domain range, equipment, and target geometry; Chapter III discusses the data processing utilized; Chapter IV presents measured results and compares those results to theoretical solutions; Chapter V discusses the cross polarized measurements. Finally, the relation between the impulse response waveform and the high frequency scattering analysis of the Uniform Theory of Diffraction is investigated, and the potential for complementary interaction between the two is demonstrated.

CHAPTER II

BROADBAND BACKSCATTERING MEASUREMENT SYSTEM

The impulse response may be measured on a time or a frequency domain range. A time domain range has two disadvantages which restrict the resolution of the measured impulse response. The first is the difficulty of generating an impulse with sufficient power and short enough duration (<20 psec) to achieve adequate spectral coverage. Assuming such an impulse can be generated, the second problem is the need for a single broadband antenna to transmit it.

A frequency domain range has three advantages over the time domain range, each of which hinges upon subdividing the total band. First, the required bandwidth need not be covered by a single antenna. Second, scaling can be used to increase the available bandwidth of the system hardware by the scale factor of the models. Third, the power capability of the radar system is greater over a restricted band. To implement this frequency band subdivision requires a certain amount of hardware flexibility, but it can be achieved with off-the-shelf microwave components.

The obvious disadvantage is that more measurements need be made in the frequency domain, and both amplitude and phase need to be stored at each frequency. A computer controlled RCS measurement system which can

speed up data acquisition makes the measurement of accurate impulse response waveforms feasible.

A broadband, frequency domain, complex radar cross section measurement range based on the concept of background nulling has been implemented for this purpose. The system is similar to that devised by Weir et al., at Stanford [18]. By circumventing the need for a time consuming background nulling at each frequency the system allows for the rapid collection of target backscatter over a wide band of frequencies. The subtraction and calibration algorithm will be explained in detail in Chapter III.

The data collection system is shown in Figures 2-1 and 2-2. Data acquisition is controlled by a Declab PDP11/03 minicomputer. The source is a Hewlett Packard 8690B microwave oscillator with interchangeable octave band modules of 1-2 GHz, 2-4 GHz, 4-8 GHz, and 8-12 GHz. No external amplification is used and output power varies from 10-70 mW depending on the module. Before each reading is taken an Autohet microwave counter checks the frequency of the output and corrects it to within a resolution of 1 MHz.

The receiver is a Hewlett Packard 8410A Network Analyzer. The received signal is a vector measured relative to a reference signal tapped off the transmit port. The Network Analyzer provides relative amplitude and phase (50 mV/dB and 10 mV/degree) as analog voltages on separate channels. The reference signal is routed through a delay line which approximates the average two-way phase path of the anechoic

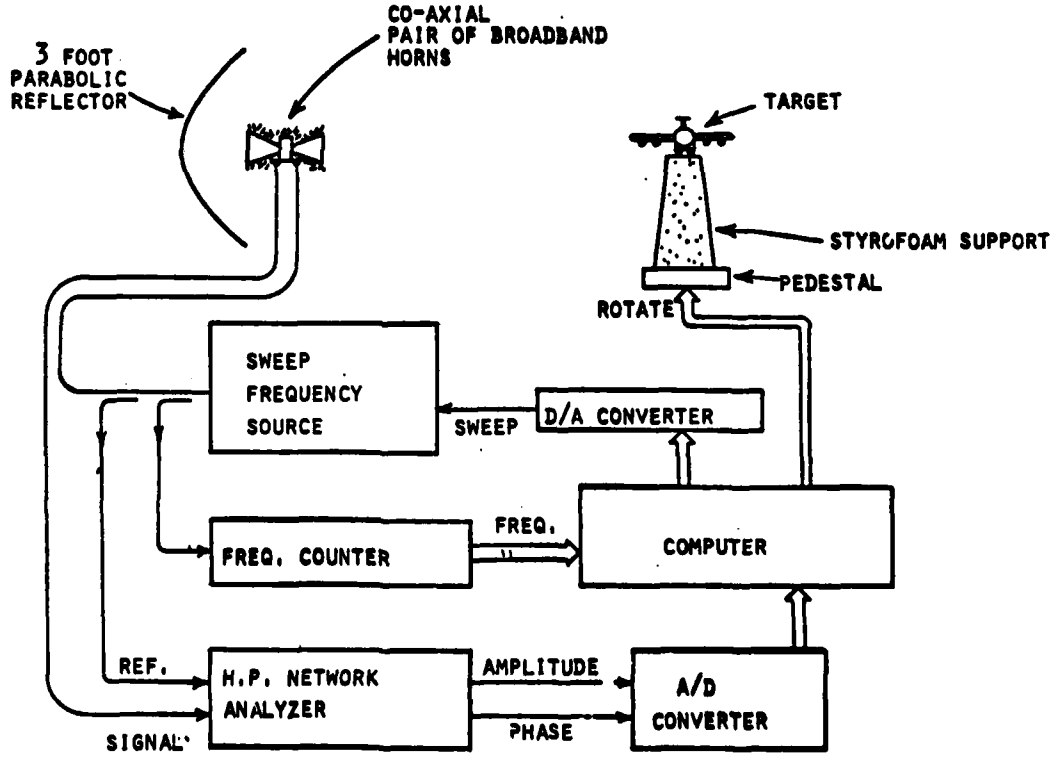

Figure 2-1. Broadband, frequency domain, complex radar cross section measurment range.

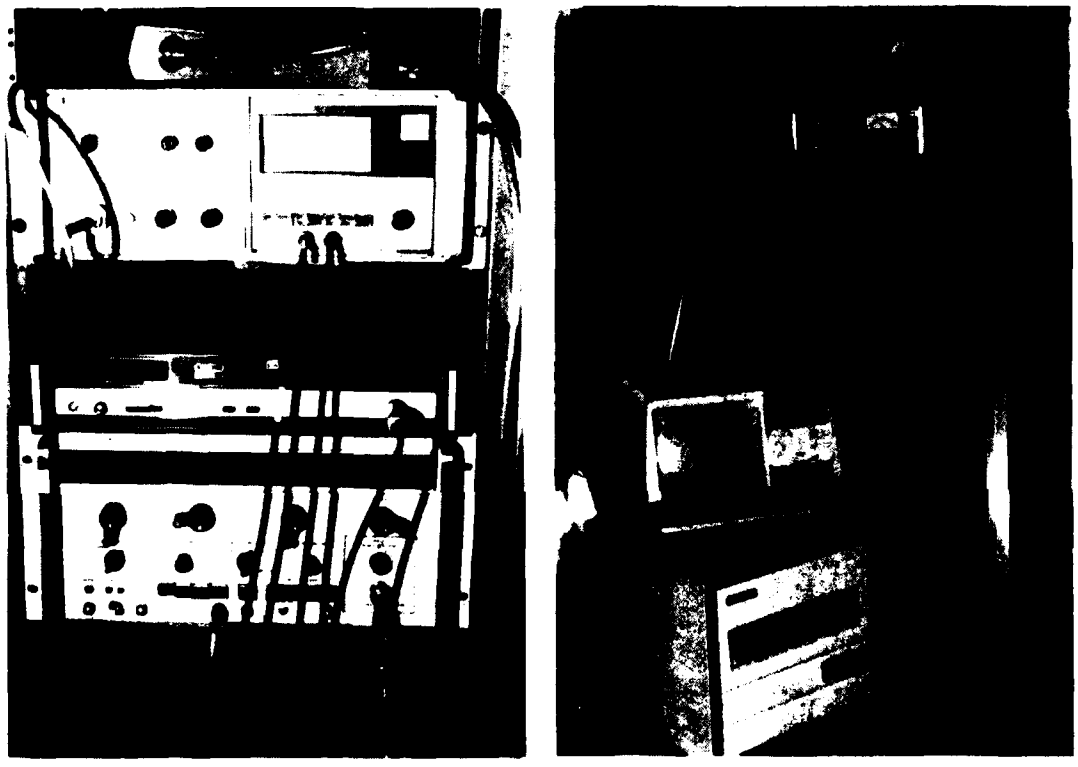

Figure 2-2. Some hardware components used in the measurement system: Hewlett Packard 8690B microwave oscillator, Hewlett Packard 8410A Network Analyzer, and Declab PDP 11/03 minicomputer.

chamber. This delay minimizes the number of phase branch cuts in the received signal relative to reference.

The measurement facility uses two broadband AEL microwave antennas mounted back to back at the focal point of a three foot parabolic reflector. Such an arrangement allows the measurement of true backscatter. The antennas and the range are shown in Figure 2-3. The transmit and receive horns are isolated with absorbing material to reduce direct coupling.

While it is not necessary to null the background with this system, it is desirable to reduce the strength of multipath returns, such as the signal scattered from the target to the floor and reaching the receive antenna. For this reason the chamber is kept as anechoic as possible. The background return, including antenna coupling, was reduced approximately 60 dB below the direct coupled signal.

The AEL microwave antennas operate from 1 to 12 GHz. The targets were constructed of cast aluminum in two scale sizes related by an 8:1 scale factor. This combination gives an effective bandwidth of 96:1, which is in the range required for accurate impulse response construction. The targets of primary interest in this study are: a 2:1 right circular cylinder, a 2:1 right circular cylinder with a hemispherical cap on one end, and a 2:1 prolate spheroid. Target geometry and actual physical dimensions are shown in Figure 2-4. The frequency ranged over $0.9 < kL < 96$, where L is the maximum target dimension and $k = 2\pi/\lambda$. Spheres ranging in diameter from 1.25 to 6.0 inches were measured over the same frequencies.

Figure 2-3. Anechoic chamber and back to back microwave antennas set up to measure true backscatter.

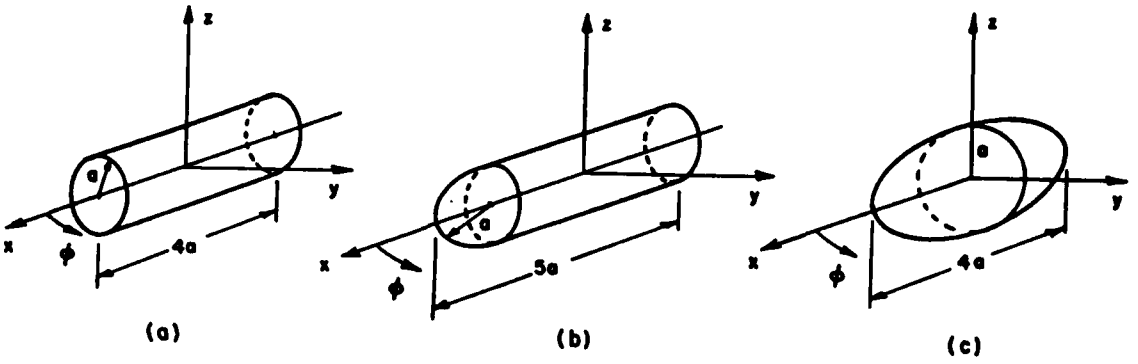

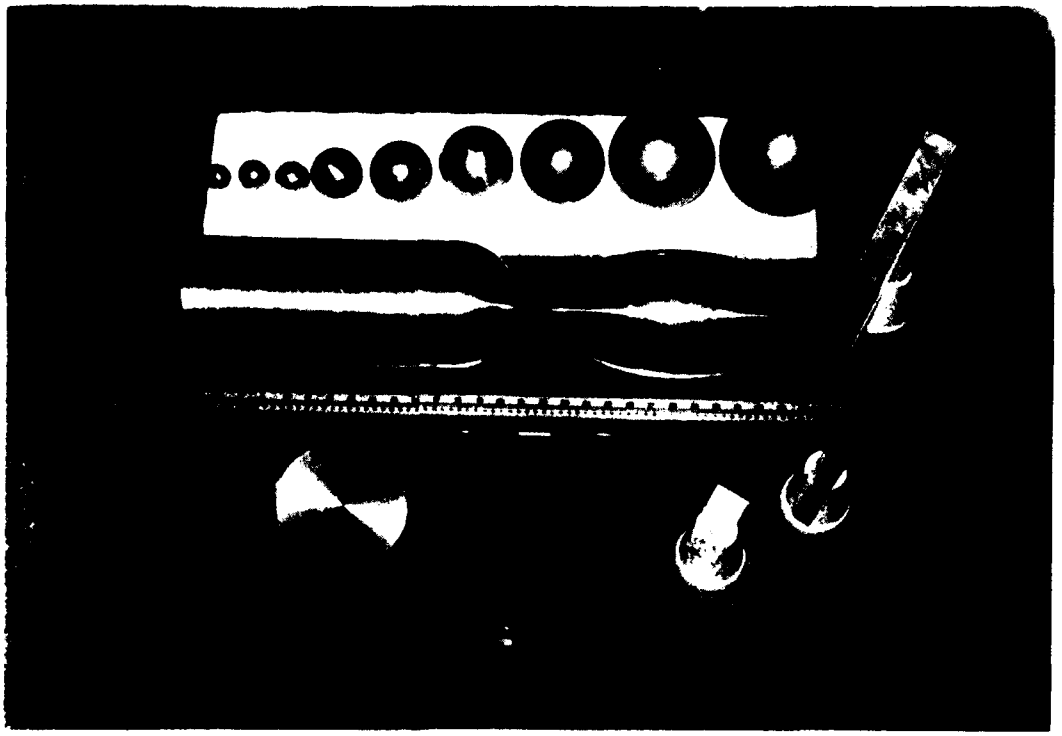

Figure 2-4. Target set:
a) 2:1 right circular cylinder of radius a.
b) 2:1 right circular cylinder of radius a with hemispherical cap.
c) 2:1 prolate spheroid.
d) calibration targets and scale targets.

The targets were mounted on a ten foot styrofoam pedestal which is rotated under computer control. Measurements were made at increments of fifteen degrees in both the E plane and the H plane. For the cross polarized measurements the target set included discs, flat plates, and strips at look angles out of the planes of symmetry. The cross polarized measurements are discussed separately in Chapter VI.

CHAPTER III

DATA PROCESSING

The discussion of data processing covers the following areas: 1) calibration of the measured data, 2) sampling criteria, 3) smoothing, 4) windowing, 5) resolution in the time domain, 6) possible sources of error, and 7) error estimation.

The calibration algorithm is given in Equation (3.1). The broadband measurement range uses background subtraction rather than background nulling. The amplitude and phase of the backscattered signal is recorded at discrete frequencies for each of three cases: 1) target plus background, 2) background only with no target, 3) calibration target plus background. The calibration target is one with a known exact complex backscatter over the frequencies of interest. For the co-polarized measurements, spheres of various sizes are used as calibration targets.

The measurments of target plus background ($\tilde{TB}$) are stepped through a set of pre-determined frequencies. Normally 201 data points are recorded over an octave band. The measurements of background with no target ($\tilde{B}$) are then stepped through the same frequencies. The process is repeated for the calibration sphere ($\tilde{CB}$). At each frequency these three sets of measured data are then combined with the exact sphere

spectrum ($\tilde{E}$) in the following algorithm:

$$\tilde{T}_C = (\tilde{TB}-\tilde{B}) \frac{(\tilde{E})}{(\tilde{CB}-\tilde{B})} \quad . \tag{3.1}$$

Since the factor $(\tilde{E})/(\tilde{CB}-\tilde{B})$ is a complex calibration constant which calibrates out the system variables, the result, $\tilde{T}_C$, is the complex radar cross section of the target alone. The problem of noise is considered in subsequent paragraphs.

When spectral data are sampled and passed through a Fast Fourier Transform (FFT), the resulting time waveform is periodic. Overlap, or aliasing, in the time waveform is a possible source of error which is avoided by proper selection of the frequency sampling interval, $\Delta\omega$. If the time domain transient response is zero for $|t| > T$, then the time waveform is accurately reconstructed by frequency samples at intervals of $\Delta\omega < \pi/T$. It is safe to assume that the transient response dies out after $T = 6\tau$, where $\tau = L/C$, L is the maximum target dimension, and C is the speed of light. Thus the frequency spectrum need only be sampled at intervals of $\Delta\omega < \pi/6\tau$, or $\Delta kL < \pi/6$, where $k = 2\pi/\lambda$.

The measured spectral data are considerably oversampled, with the sampling rate ranging from five times to one hundred times the minimum rate. A total of 1401 unequally spaced frequency samples are distilled prior to the FFT to kL samples at intervals of $\Delta kL = 1/10$, which is 5.24 times the minimum rate. This sampling interval fixes the total time frame at 63τ.

Oversampling justifies smoothing to improve the accuracy of the measured spectral data. At each sample point, a smoothed phasor value is found by weighting the real and imaginary parts of the (N-1)/2 adjacent samples on either side of it with a shifted cosine. The weighting function is

$$w(n) = 0.5[1.0 + \cos(2n\pi/N)],\ n= -(N-1)/2, \ldots, 0, \ldots(N-1)/2\ , \tag{3.2}$$

with the sum of the weights equal to N.

The number, N, of samples averaged varies from 5 to 25 depending on frequency. Moving the weighting function across the frequency samples is a convolution in the frequency domain. This is equivalent to multiplication in the time domain by the inverse transform of w(n), which is shown in Figure 3-1 for N=15. The target information lying in a 6τ time frame centered at t=0 is passed unattenuated, while the range clutter lying outside $\pm 6\tau$ is effectively removed. Smoothing thus serves to improve the accuracy of the samples through averaging, as well as to time gate some undesired signals.

In Equation (3.1) the difference phasors, $(\tilde{TB}-\tilde{B})$ and $(\tilde{CB}-\tilde{B})$, both contain noise. It has been found that smoothing both difference phasors before division inhibits the multiplication of noise inherent in the division. This operation requires that the range phase, e^{-j2kR}, be factored out of both numerator and denominator, or equivalently, that the difference vectors be centered in the time window shown in Figure 3-1. Some pre-smoothing of the phase has also been found to improve the

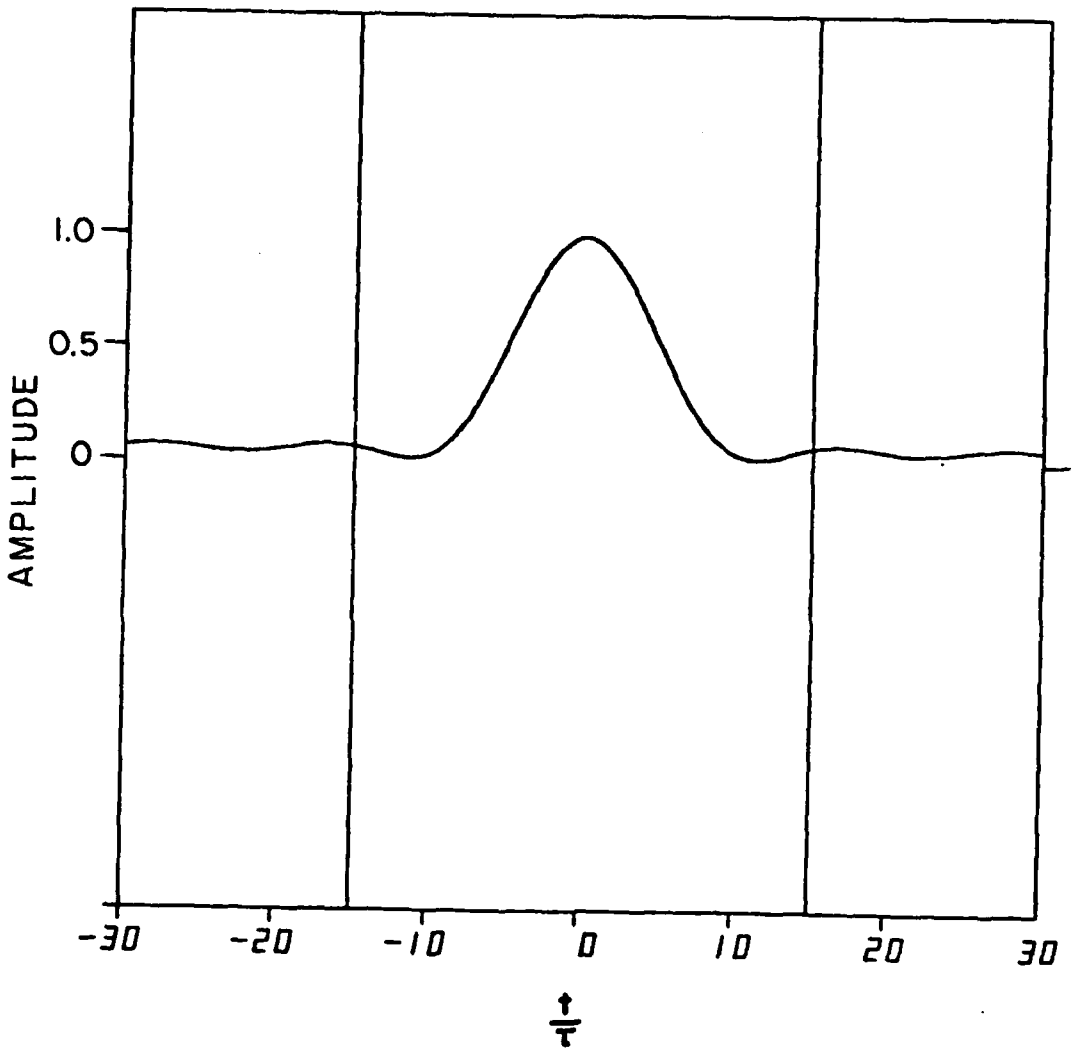

Figure 3-1. Inverse Fourier transform of the frequency domain weighting function, $\frac{1}{2} + \frac{1}{2}\cos(2n\pi/N)$, for N = 15. Unit of τ=L/C where L = maximum target dimensions, and C = speed of light.

results, especially in those parts of the spectrum where phase branch cuts occur.

Windowing of the frequency domain data is used to reduce the Gibb's phenomenon caused by truncation of the measured spectrum. Hanning, Hamming, Gaussian, and Tukey windows have been implemented for this purpose. The Hanning window has been found to give the best overall results. The weighting function for the Hanning window is the same as that given in Equation (3.2) except that the weighting is applied across the entire spectrum. Such multiplication in the frequency domain is equivalent to convolution in the time domain. The inverse transforms of the various windows are given in [19] along with their performance characteristics. In particular, the highest sidelobes of the transform of the Hanning window are -32 dB as compared to -13 dB for the sin(x)/x transform of the rectangular window. The improvement in sidelobe level is in exchange for a 50 percent increase in the equivalent pulse width from 0.066 τ for the rectangular window to 0.10 τ for the Hanning window. The inverse transform of the Hanning window is shown in Figure 3-2 for kL < 96.0. On the linear amplitude scale the sidelobes are barely discernable.

The equivalent pulse width discussed above is a measure of the resolution of the time domain waveforms. The resolution is fixed by the maximum frequency of the samples. For the 15 inch target we will examine in Chapter IV, τ = 1.27 nsec, and for a maximum sampling frequency of 12 GHz the equivalent pulse width is 0.0833 nsec, increasing to 0.127 nsec when the Hanning window is applied. The time

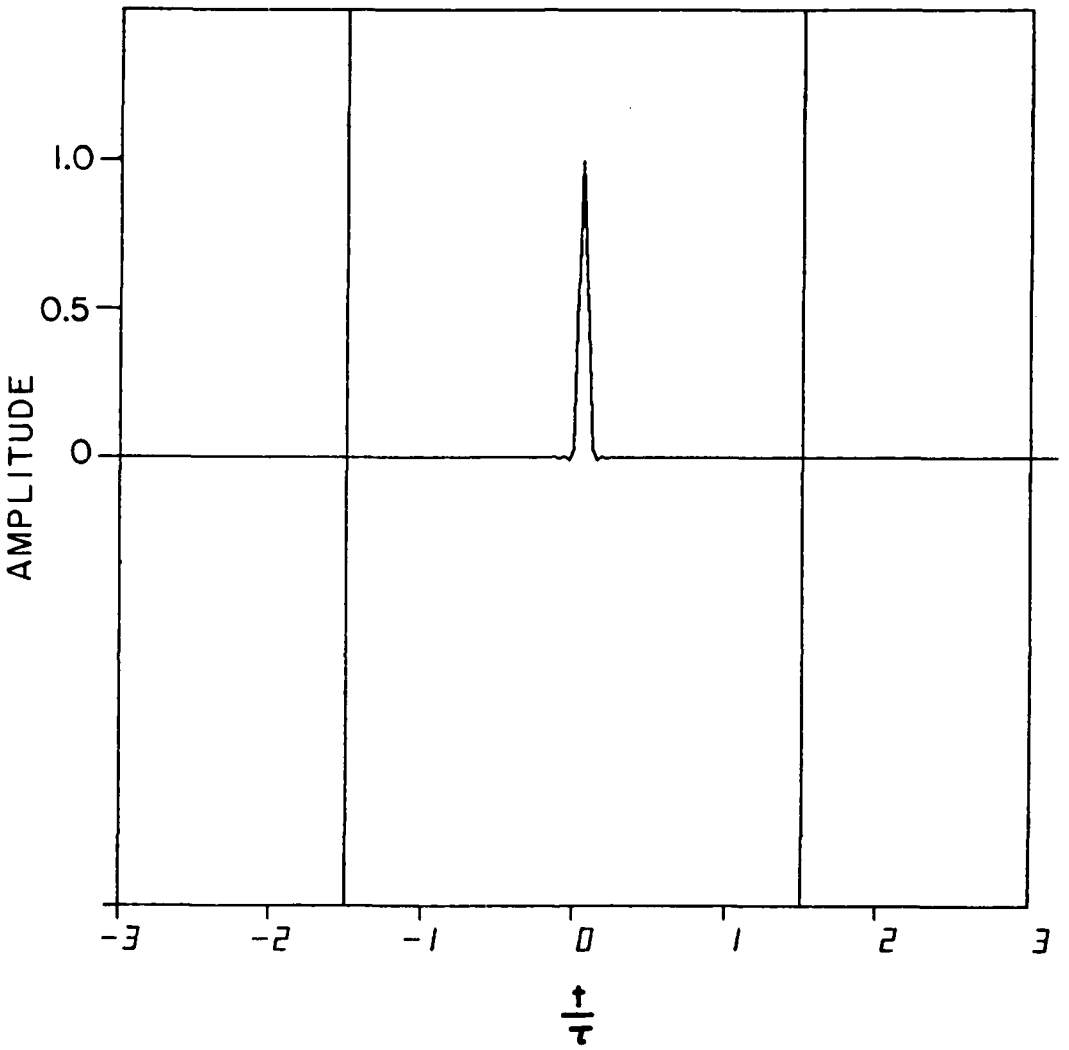

Figure 3-2. Equivalent pulse width for highest frequency sample of kL=96.0, with Hanning window applied. Units of τ=L/C where L = maximum target dimension, and C = speed of light.

scale in Figure 3-2 may be used as a reference for the resolution in the waveforms to be presented in Chapter IV.

Before moving on to a discussion of noise one last point is worth noting. Since the measurements extend well into the Rayleigh region it is possible to apply a least squares fit to the first 200 samples, from which a Rayleigh coefficient may be extrapolated. This allows the spectrum to be extended down to the first harmonic at kL = 0.1, thereby fitting the lower harmonics and eliminating the discontinuity at kL = 1.0.

Besides those already mentioned, other possible sources of measurement error are system noise, multi-path scattering, and target positioning error. System noise includes amplifier noise in the receiver front end and in the A-D converters and frequency drift. A figure of merit for system noise is the noise floor. The noise floor is measured by treating a background measurement as a target in Equation (3.1) and subtracting another background measurement, taken during the same data run. The result is essentially a repeatability test. The two background measurements are taken at the beginning and end of a data session so as to include the effects of drift. A typical noise floor of between 0 and 5 dB>cm^2(-40 to -35 dBsm) is shown in Figure 3-3. The resulting phase should be random.

Error due to multi-path scattering from the target to some part of the chamber, and finally to the receive antenna is reduced by making the chamber as anechoic as possible. The background scattering was reduced approximately 50-60 dB with absorbing material. In particular, the

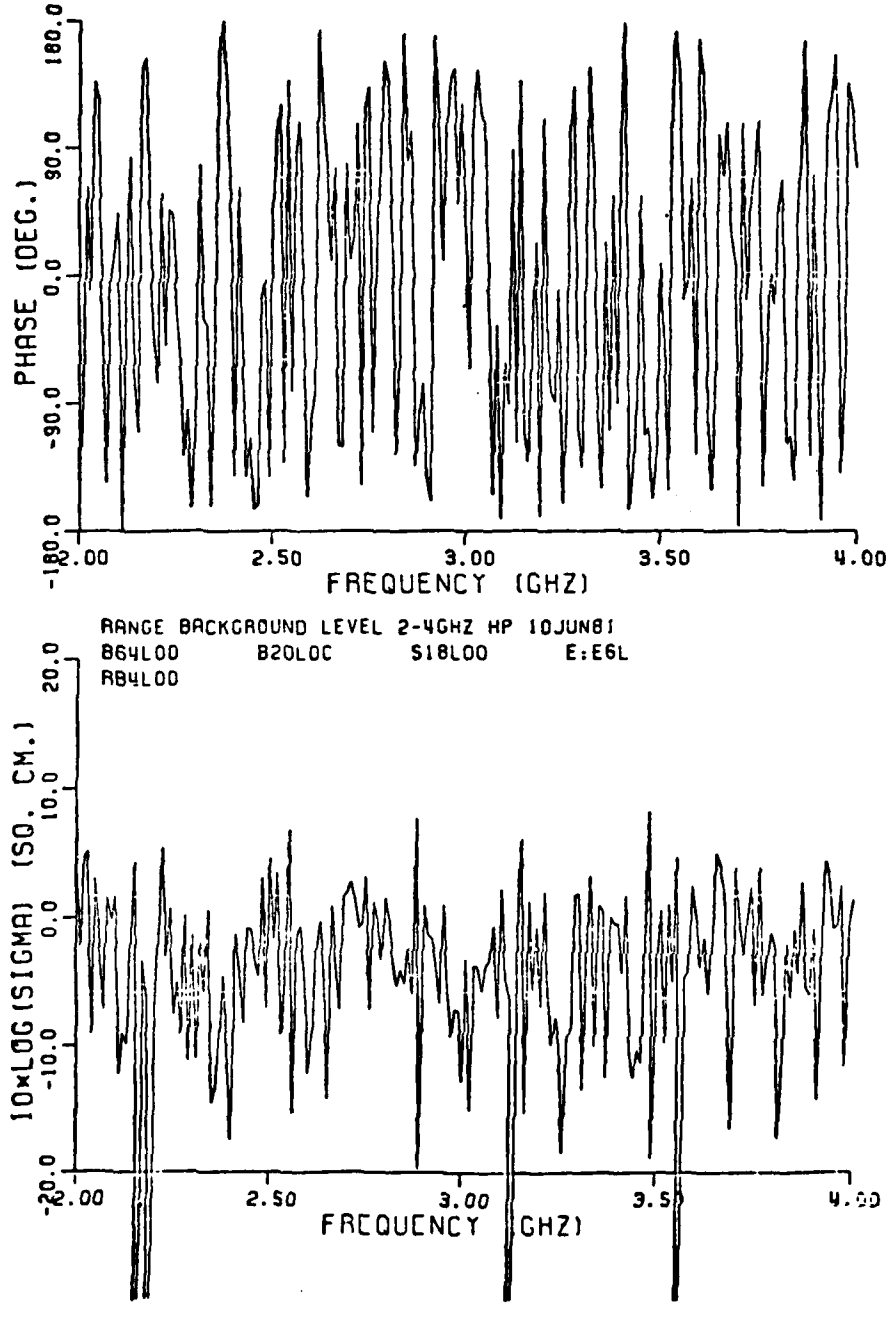

Figure 3-3. Typical noise floor in dB>cm^2.

direct coupling between transmit and receive horns was reduced by wrapping them with absorber, as can be seen in Figure 2-3.

Target positioning error may corrupt the measured phase data. It has been found that the positioning is accurate for frequencies up to 8 GHz, and adjustments need be made only in the 8-12 GHz band. The correcting procedure is to inverse transform the measured 8-12 GHz spectra separately before combining with the lower frequency data. If the scattering from the specular point is used as a reference on the time axis the target can be "moved" to proper alignment position by a simple time shift. This is equivalent to matching the slope of the phase at the 8 GHz junction.

Finally, an estimate of the total measurement error has been performed to place reliability bounds on the data. Applying a single, one-dimensional error figure to broadband, complex data is not valid since the measurement error varies with target cross section, frequency, and coherency of the amplitude and phase data.

In an early attempt at placing error bounds on the data a large number of samples were taken at a single frequency for each of the terms in Equation (3.1), and run through the calibration algorithm. Standard deviations about the means were calculated for amplitude and phase separately. The procedure was repeated for targets with cross sections ranging from 40 dB>cm^2 down to 10 dB>cm^2, and at several frequencies. The resulting error estimates ranged from ±0.5 dB and ±4.0° for target cross sections above +25 dB>cm^2 to ±1.7 dB and ±10° for target cross sections of +10 dB>cm^2. It should be noted that these figures are for

unsmoothed data and thus do not reflect the processing discussed earlier. These early estimates are quoted in [20].

A more accurate error estimate is obtained in the time domain. Besides treating amplitude and phase coherently, a time domain analysis includes the effect of smoothing and all possible sources of error. In this analysis the measured data for a sphere are compared to exact sphere data. There are several reasons for using the sphere error as representative of all measurement error. The sphere is used to calibrate all the co-polarized measurements; the cross section of the sphere is lower than that of the larger targets of interest; and the sphere has an exact spectrum from which to calculate measurement deviation.

Figure 3-4 shows the exact and measured spectra for the sphere. The measured spectrum is offset +10 dB. A Gaussian taper has been applied to the highest harmonics to eliminate the sharp truncation at 12 GHz, but no windowing has been done across the midband. The corresponding phase information is shown in Figure 3-5. Both spectra are inverse transformed and the difference taken between the time waveforms. This difference is then transformed to give the error spectrum in Figure 3-4. The vertical scale is in dB below the physical optics cross section for the sphere. The -20 dB level corresponds to 1 percent error or ±0.04 dB. It can be seen that throughout most of the band the measurement error falls below the 1 percent level. The worst case error is at -12 dB corresponding to a 5 percent error or ±0.25 dB. This occurs at frequencies below 1 GHz and for one peak at 3 GHz.

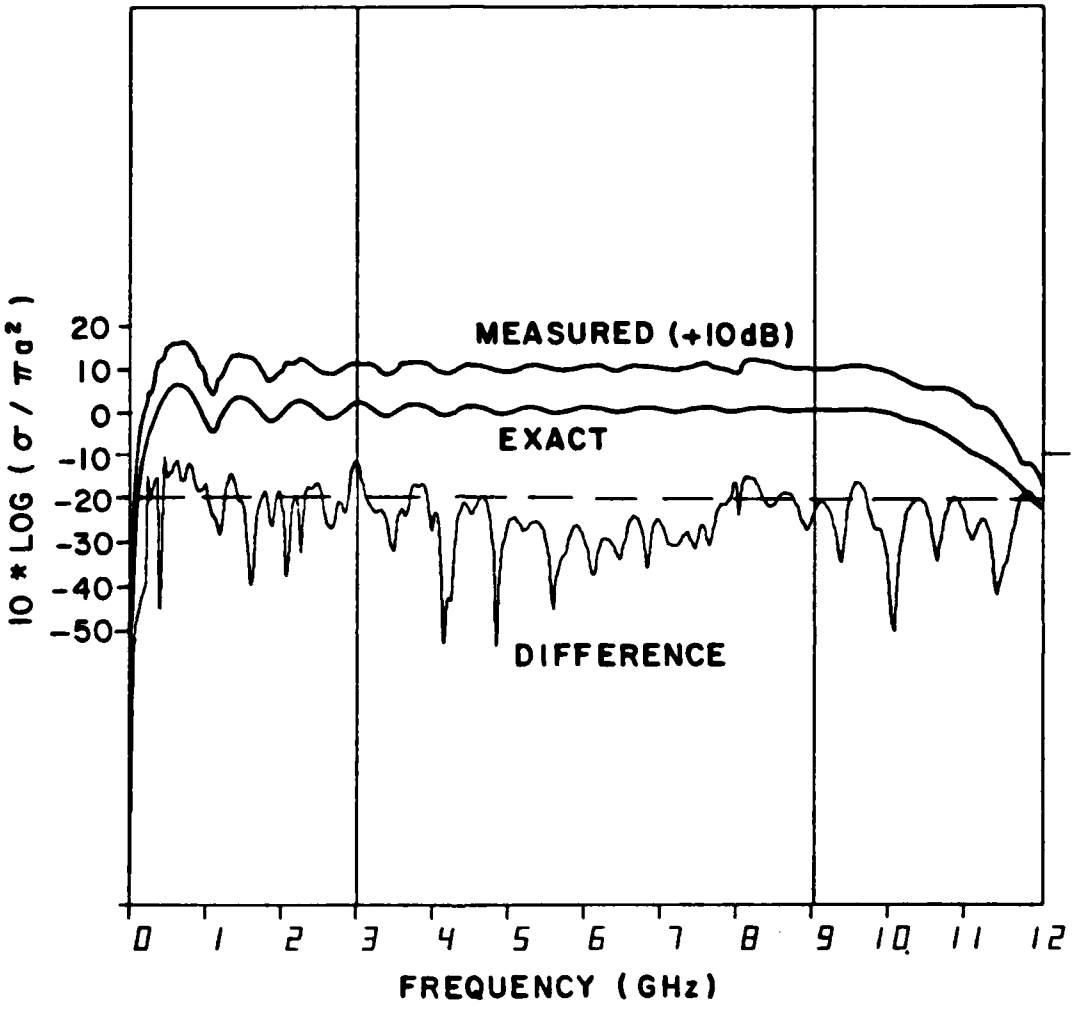

Figure 3-4. Upper curve: measured sphere spectrum offset +10 dB.
Middle curve: exact sphere spectrum.
Lower curve: spectrum of difference between measured and exact.
Vertical scale: radar cross section in dB > πa^2 for a = sphere radius = 7.62 cm.
Horizontal scale: frequency in GHz.

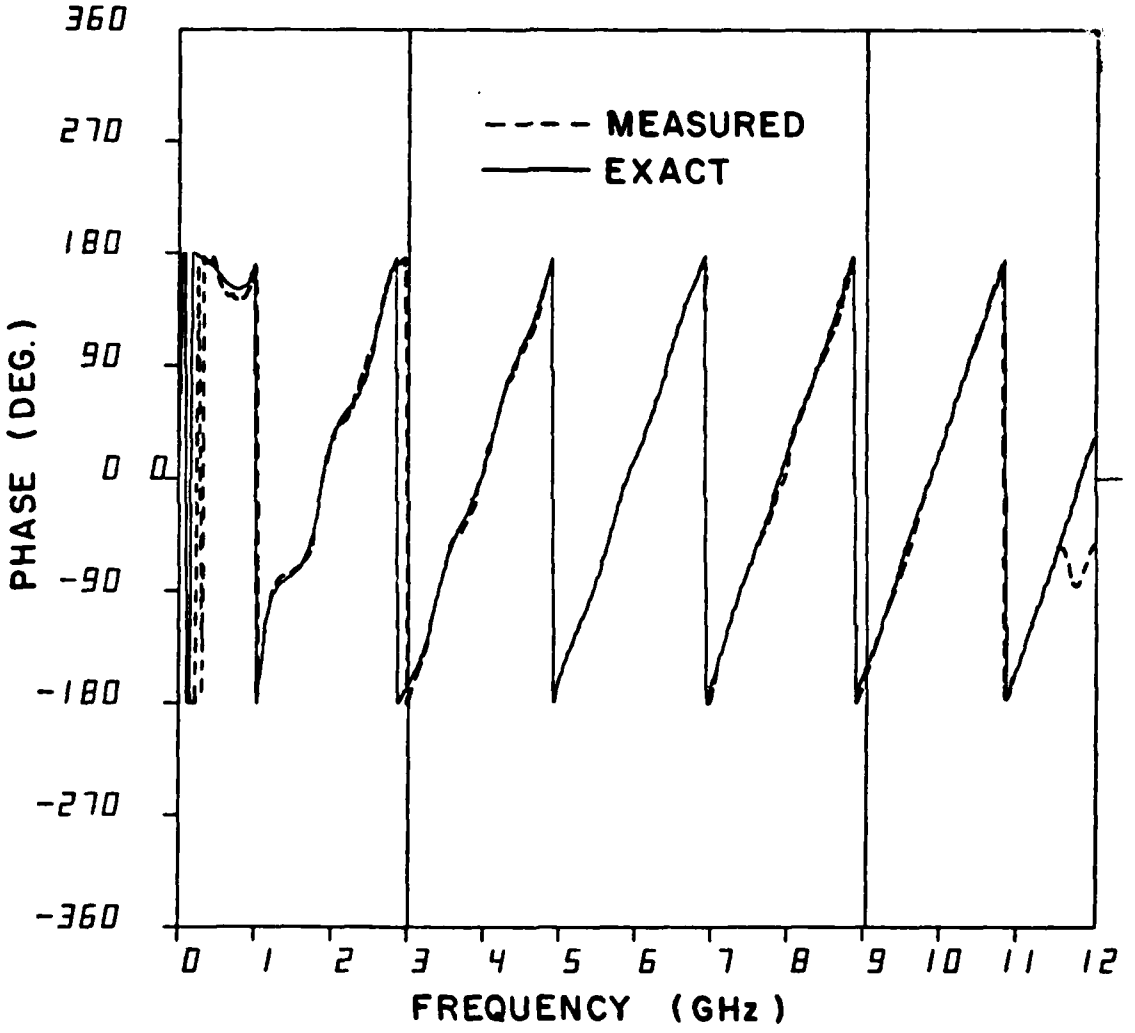

Figure 3-5. Measured versus exact phase of sphere with radius, a = 7.62 cm.

In the low frequency region the error is due to the generally lower cross section of the targets combined with the difficulty of measuring phase as it hovers around 180°. At 3 GHz the amplitude spectra compare very well, but Figure 3-5 shows a phase error near a branch cut. This illustrates that the time domain error analysis includes the effect of phase coherently.

To demonstrate that the improved error performance shown in Figure 3-4 is due to smoothing we may compare it with the error estimates for unsmoothed data given earlier. One would expect the standard deviation for the unsmoothed data to be reduced by a factor $1/\sqrt{N}$, where N is the number of samples included in the smoothing. A standard deviation of 0.5 dB in the unsmoothed data corresponds to an error of 22 sq. cm. for a six inch diameter sphere with physical optics cross section of 182 sq. cm. If a 21 point smoothing is applied, this error is reduced to 4.85 sq. cm., which is 16 dB down from the physical optics cross section. This figure is closer to the error estimate in Figure 3-4.

In summation, the measured data is accurate to within 1 percent or better over most of the spectrum. This figure can be applied to phase and amplitude together, and includes all possible sources of error.

CHAPTER IV

MEASURED IMPULSE RESPONSES

The impulse response of a scattering object is a time domain concept derived from linear systems analysis [1]. With the input defined to be the linearly polarized field incident upon the scatterer the output is taken to be a selected component of the scattered field in a particular direction. The derivation of the impulse response concept applied to E.M. scattering will be briefly summarized here as will the physical optics approximation to the impulse response of a few simple shapes.

The radar cross section, σ, of a scattering object is a frequency domain concept defined as

$$\sigma \doteq 4\pi r^2 \left| \frac{E^s(j\omega)}{E^i(j\omega)} \right|^2 \quad . \tag{4.1}$$

where $E^s(j\omega)$ is a selected polarization component of the scattered electric field at a distance r from the object and $E^i(j\omega)$ is the linearly polarized electric field incident upon the object. The geometry of the scattering problem is sketched in Figure 4-1. The scattering object lies at the coordinate origin.

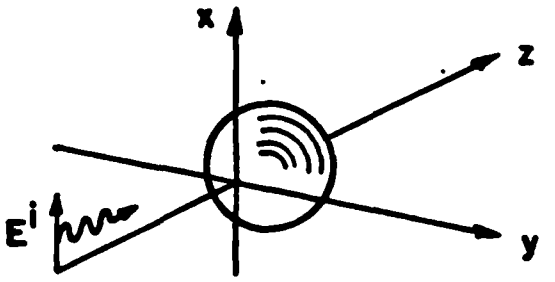

$$E^i = \hat{x}\, E(t-z/c)$$

Figure 4-1. The geometry of the scattering problem.

We will assume the case of backscatter and $r>>\lambda$. While these assumptions are not necessary for the general derivation of the impulse response they are implied in the use of σ.

So long as we restrict the polarization of the incident and scattered fields to a single component, the scalar ratio $E^s(j\omega)/E^i(j\omega)$ is just a linear system transfer function. If we define a normalized transfer function, $F(j\omega)$, as

$$\text{Re}\left\{F(j\omega)e^{j\omega(t-r/c)}\right\} = \frac{2r}{c}\,\frac{E^s(t-r/c)}{E^i(0)}\,,\quad E^i = \hat{x}\cos\omega(t-z/c), \qquad (4.2)$$

then

$$\sigma = \pi c^2\,|F(j\omega)|^2 \qquad . \qquad (4.3)$$

The normalized transfer function, $F(j\omega)$, has a unique inverse Fourier transform which is the time response of the scatterer. If the incident field is an impulse, $\delta(t-z/c)$, the time response is the impulse response, $F_I(t)$. To make sense physically we must require that the scattering problem be causal, that is, there can be no scattered field before the incident field reaches the nearest point on the scatterer. In other words, $F_I(t)$ is identically equal to zero for all $t<0$, and we have the transform relation,

$$F(j\omega) = \int_0^\infty F_I(t)\, e^{-j\omega t}\, dt \quad . \tag{4.4}$$

The time response of a scatterer to an arbitrary input waveform may be obtained by convolution with $F_I(t)$. Thus the impulse response summarizes the response of a scatterer to all interrogating waves at all frequencies. The impulse response concept can be applied to scatterers of any material although we will limit the discussion to perfect conductors.

Some useful properties of the impulse response can be derived from the behavior of the scattered field in the low frequency (Rayleigh) limit and in the high frequency (physical optics) limit. The first three moment conditions on $F_I(t)$ are obtained by enforcing the Rayleigh law of scattering on $F(j\omega)$ [4].

$$\int_0^\infty F_I(t)\, dt = 0 \quad . \tag{4.5}$$

$$\int_0^\infty tF_I(t)\, dt = 0 \quad . \tag{4.6}$$

$$\int_0^\infty t^2 F_I(t)\, dt = 2a_2 \quad , \tag{4 7}$$

where a_2 is the coefficient of ω^2 in an expansion of $F(j\omega)$ near $\omega = 0$. From Equation (4.5) we see that the net area beneath the impulse response waveform is zero.

In the high frequency limit the current distribution over the illuminated portion of the scatterer can be approximated by $2\hat{n} \times H^i$. The resulting physical optics approximation to the impulse response is

$$F_I(t) = -\frac{1}{4\pi}\frac{d^2A(z)}{dz^2} \quad , z = \frac{ct}{2} \quad , \tag{4.8}$$

where $A(z)$ is the cross sectional area intercepted by a plane at z parallel to the xy plane and travelling in the positive z direction at a speed equal to one-half the velocity of the incident wave. $A(z)$ is zero for $z<0$ and increases monotonically to a constant value at the incident shadow boundary.

The physical optics approximation to $F_I(t)$ is insensitive to the polarization of the incident field, erroneously predicts a discontinuity in $F_I(t)$ at the shadow boundary, and does not predict any creeping wave contribution. But, in keeping with the final value theorem of the Laplace transform, the high frequency approximation to $F(j\omega)$ properly predicts the behavior of $F_I(t)$ near $t = 0$. Thus it provides a good first order approximation which can be corrected using the moment conditions and information about creeping wave behavior. A much more accurate approximation may be obtained from the Uniform Theory of Diffraction.

Because of the simple relation between the physical optics approximation to $F_I(t)$ and the geometry of the scattering object it is instructive to derive the physical optics approximation for a few simple shapes. A sphere, a right circular cylinder, and a disc represent three types of surface curvature. The sphere has a finite radius of curvature in both principal planes. At broadside the cylinder has an infinite radius of curvature in one principal plane and the disc has infinite radii of curvature in both. It is therefore interesting to compare the impulse response of each near $t = 0$. The physical optics approximations to the impulse response of these three scatterers are derived in Appendix A and illustrated in Figure 4-2. For convenience the time axis is given in units of t/τ where τ equals the two way free space transit time required to travel a distance 2a, and a is the radius of the sphere, cylinder, and disc.

For the sphere (Figure 4-2a) physical optics predicts a negative impulse of strength a/c followed by a positive step of height 1/2 and duration τ. Correction to this first order approximation will be discussed shortly.

Figure 4-2b gives the physical optics approximation to the impulse response of a 2:1 right circular cylinder of radius a at broadside incidence. At time $t = 0$ a negative impulse is followed by a positive jump discontinuity which drops rapidly to a constant level of $2/\pi$. The positive portion of $F_I(t)$ for $0 < t < \tau$ behaves as $\frac{2}{\pi} \tau^3 \left[2\tau t - t^2\right]^{-3/2}$

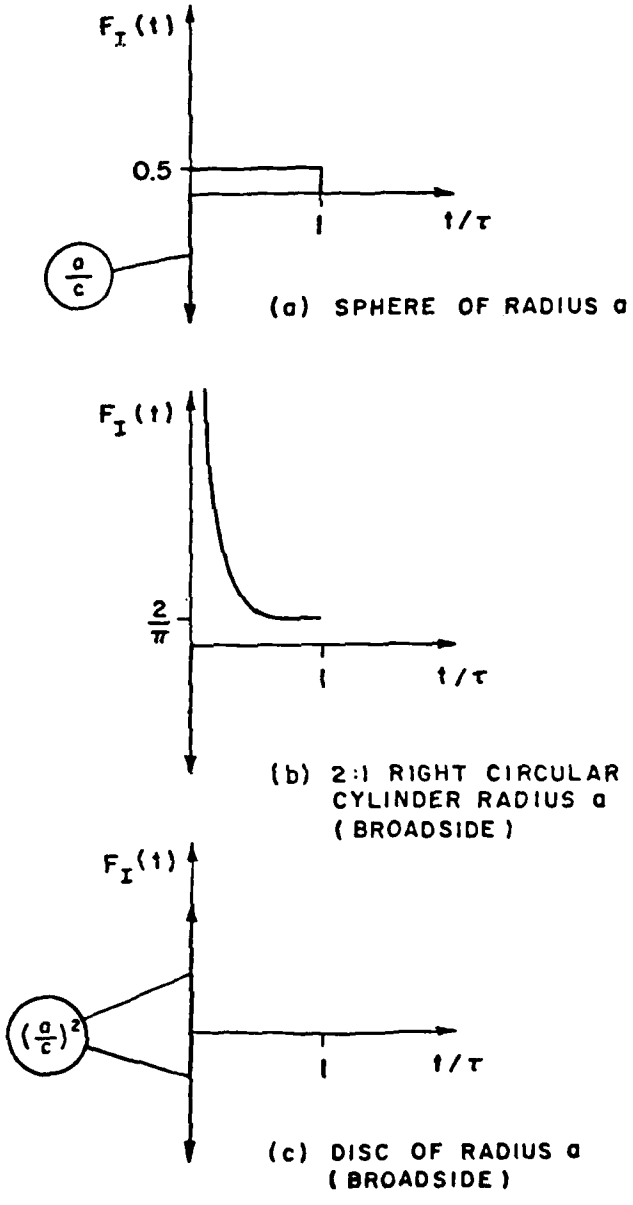

Figure 4-2. Physical optics approximation to the impulse response of three simple shapes representing three types of surface curvature at the specular.

where $\tau = 2a/c$. As t approaches 0^+ the singularity is of the order $\frac{1}{\sqrt{2\pi}} \left(\frac{\tau}{t}\right)^{3/2}$. Since the positive excursion does not enclose a finite area in zero time we do not have a true doublet t = 0.

In Figure 4-2c the physical optics approximation to $F_I(t)$ for the disc at broadside is shown to be a doublet of strength $\left(\frac{a}{c}\right)^2$. Of interest here is the progression in the overall shape of $F_I(t)$ due to the change in surface curvature at the specular point. These three types of behavior will be exhibited in the measured impulse responses.

Improvements over the physical optics approximation to $F_I(t)$ have combined some rather ingenious time domain techniques [3] with available spectral solutions [4], [7]. The Geometrical Theory of Diffraction has played a key role. The high frequency solution is able to generate complex spectral data across a wide enough band of harmonics without excessive computational effort. If all significant scattering centers are included in the GTD solution all but the low frequency geometrical resonances can be recovered in the impulse response.

A corrected approximate impulse response for the perfectly conducting sphere is reproduced from [4] in Figure 4-3. The figure compares the physical optics approximation with that obtained by an inverse Fourier transform of 475 harmonics from an exact eigenfunction solution. The shape of the creeping wave may be interpreted from a UTD analysis. All creeping wave paths pass through a point on the shadowed side of the sphere which is caustic for the far field. The minimum path gives the time of the creeping wave peak at $t_{cw} = (2+\pi)a/c = 2.57\tau$. The

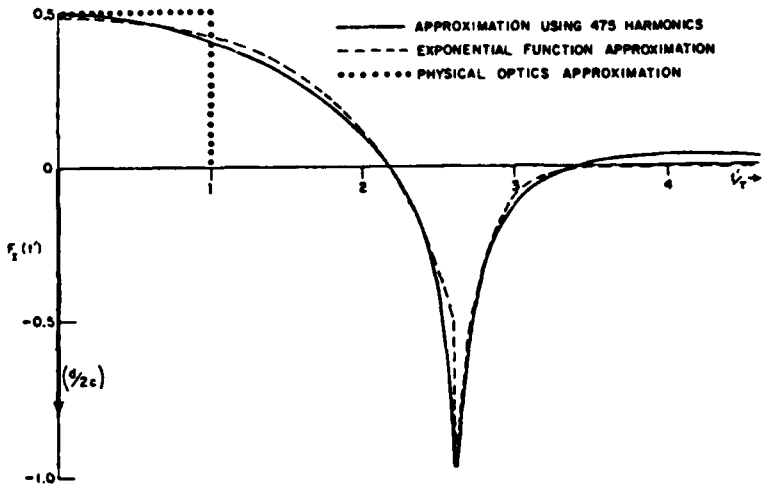

Figure 4-3. Approximate impulse response of a conducting sphere. Reproduced from [4].

trailing portion is time delayed due to the phase factor, $\exp[-\alpha_n(\omega)]$, found in the UTD expression for the creeping wave [17]. The precursor to t_{cw} is explained by the fact that the UTD phase factor, $e^{j\pi/2}$, due to crossing the caustic becomes frequency dependent [24] at lower frequencies where UTD is no longer applicable. The combined effect is the characteristic cusp shape exhibited in Figure 4-3.

Before presenting measured impulse responses we must note a shift in the time axis convention in the measured waveforms. For convenience in mounting and rotation the phase center is taken to be the center of mass of the scatterer. This results in a time shift so that time $t = 0$ corresponds to the physical center of the object. The relation to the time axis in the theoretical waveforms is obvious and should result in no confusion.

The measured impulse response for the sphere is presented in Figure 4-4 along with an inverse transform of the exact eigenfunction solution covering the same bandwidth as the measurements. The negative specular impulse, the positive step, and the creeping wave are all clearly visible. The positive overshoot at the leading edge of the step is a Gibb's phenomenon due to truncation of the spectrum. The corresponding spectra are shown in Figures 3-4 and 3-5.

A scatterer which exhibits all three types of surface curvature is the right circular cylinder with a hemispherical cap on one end. The geometry is shown in Figure 2-4. The time axis of the measured impulse response waveforms is scaled such that $\tau = 5a/c$ is the time required to travel the total length, 5a, of the sphere-capped cylinder. The case of

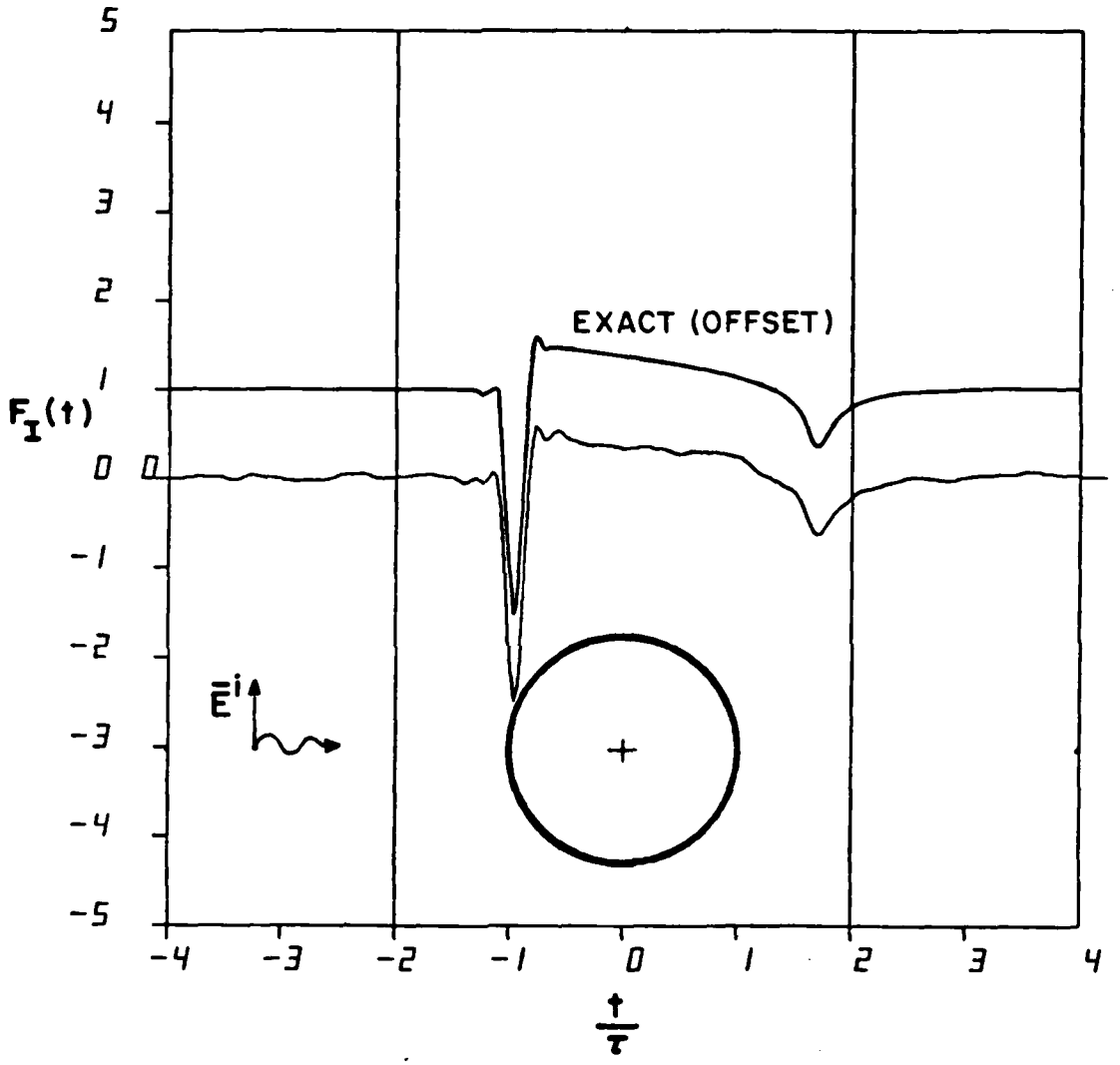

Figure 4-4. Measured impulse response of a conducting sphere compared to inverse transform of exact solution. Time axis in units of $\tau = 2a/c$ where a is sphere radius.
Bandwidth: 383 harmonics for $0.4 < ka < 19$.

axial incidence on the spherical end is taken to be the 0° case while the flat end is 180°.

The 0° case is presented in Figure 4-5. Up to time $t = \frac{2a}{c} = \frac{2}{5}\tau$ after the specular return the behavior is identical to that of the sphere. But then the waveform drops rapidly to zero along the cylindrical sides until the incident field reaches the rear edge. The positive spike is the direct diffraction from the rear edge and the negative excursion is the doubly diffracted ray which crosses the rear disc diameter. The peak of the negative term occurs at a time $\frac{2}{5}\tau$ after the positive spike, which is the time required for crossing one disc diameter. The doubly diffracted ray picks up a phase term $e^{j\pi/4}$ from each of the two diffractions and another $e^{j\pi/2}$ in crossing the caustic on the cylinder axis. This gives it a polarity opposite to that of the single diffraction. With respect to the time resolution shown in Figure 3-2, note that the singly diffracted component is of minimum width, indicating it has been diffracted as if from a single stationary point, while the doubly diffracted component exhibits the time dispersion connected with crossing the caustic on the cylinder axis.

The measured impulse response of the sphere-capped cylinder may be compared to a theoretical approximation obtained by a space-time integral equation approach [8]. In this technique the $\vec{H}$-field integral equation is solved in the time domain for the surface currents on the scattering object, and the currents then used to compute the scattered field. An impulse response augmentation technique [8] can then be used to improve the quality of the singular (high frequency) portions of the

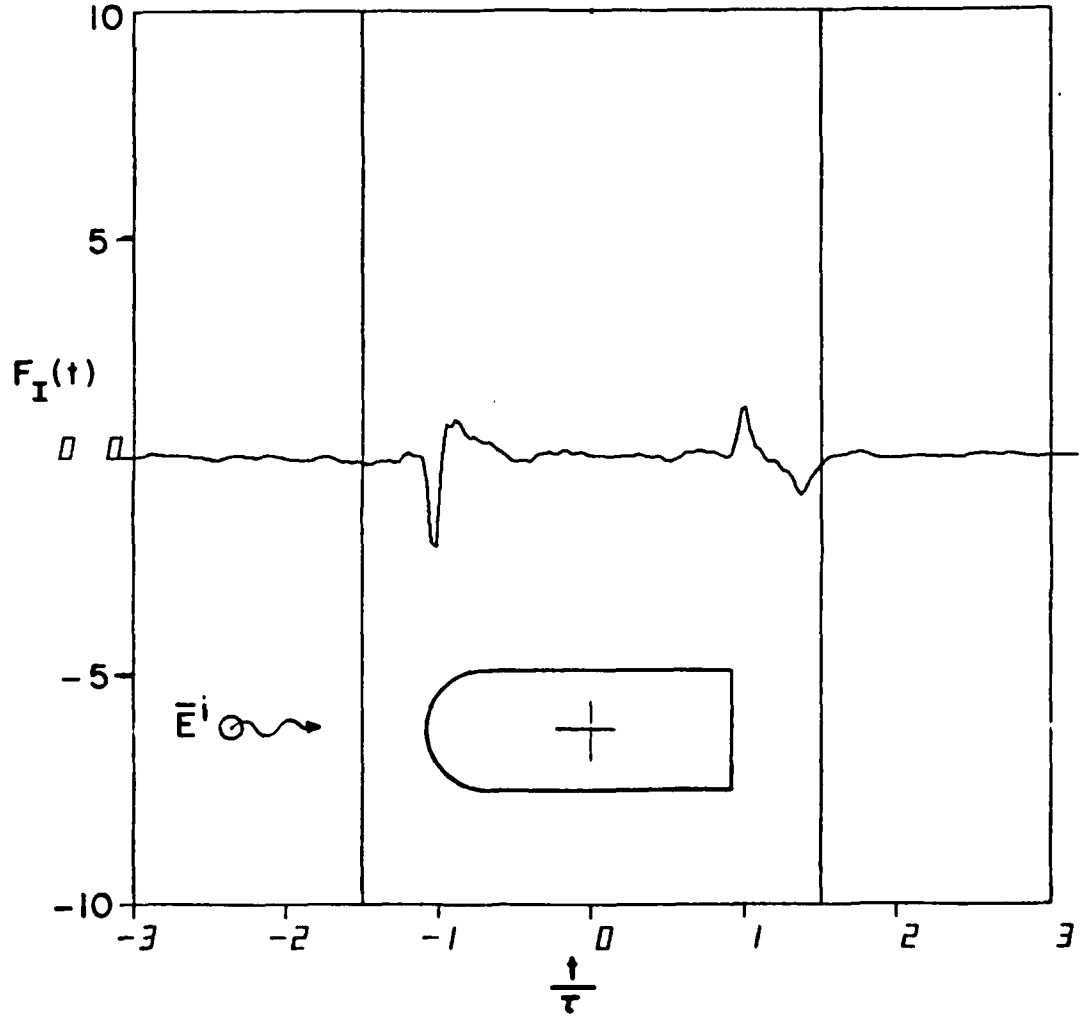

Figure 4-5. Measured impulse response of a conducting 2:1 right circular cylinder with hemispherical cap on one end. 0° case: axial incidence on the sphere-capped end. Time axis in units of $\tau = 5a/c$ where $L = 5a$ is the total length.
Bandwidth: 960 harmonics for $1 < kL < 96$.

scattered waveform. The resulting impulse response for axial incidence on the sphere-capped end is shown in Figure 4-6a. The comparison with the measured results in Figure 4-5 is quite favorable except for the relative magnitude of the two diffracted components from the rear edge. Again note the difference in the widths of these two components.

Turning now to axial incidence on the sphere-capped cylinder at 180°, the specular surface is a flat disc. The measured impulse response at 180° is presented in Figure 4-7. As expected from the physical optics approximation the specular return from the flat end of the cylinder is a doublet. But following the specular and ringing for a duration of at least 2τ appears a wave with a resonant time between positive and negative peaks of $2a/c$, corresponding to one disc diameter. Even the creeping wave, which we at expect at a time $t_{cw} = (10 + \pi)a/c = 2.6\tau$ after the specular, appears distorted by this ringing. We would expect the creeping wave to be comparable in shape and magnitude to that from a sphere of the same radius (shown in the inset), since the cylinder walls should have little effect on the field.

An equivalent currents solution [9] for the backscatter from a perfectly conducting circular disc of radius a at normal incidence gives a scattered field transfer function,

$$F(s) = \left(\frac{a}{c}\right)^2 s + \frac{1}{\sqrt{\pi}} \left(\frac{a}{c}\right)^{\frac{1}{2}} s^{\frac{-1}{2}} e^{-j\left(\frac{2a}{c}\right)s} \quad , \quad s = j\omega \quad . \tag{4.9}$$

Using the Laplace transform pair,

$$\frac{1}{\sqrt{\pi t}} \longleftrightarrow \frac{1}{\sqrt{s}} \quad , \tag{4.10}$$

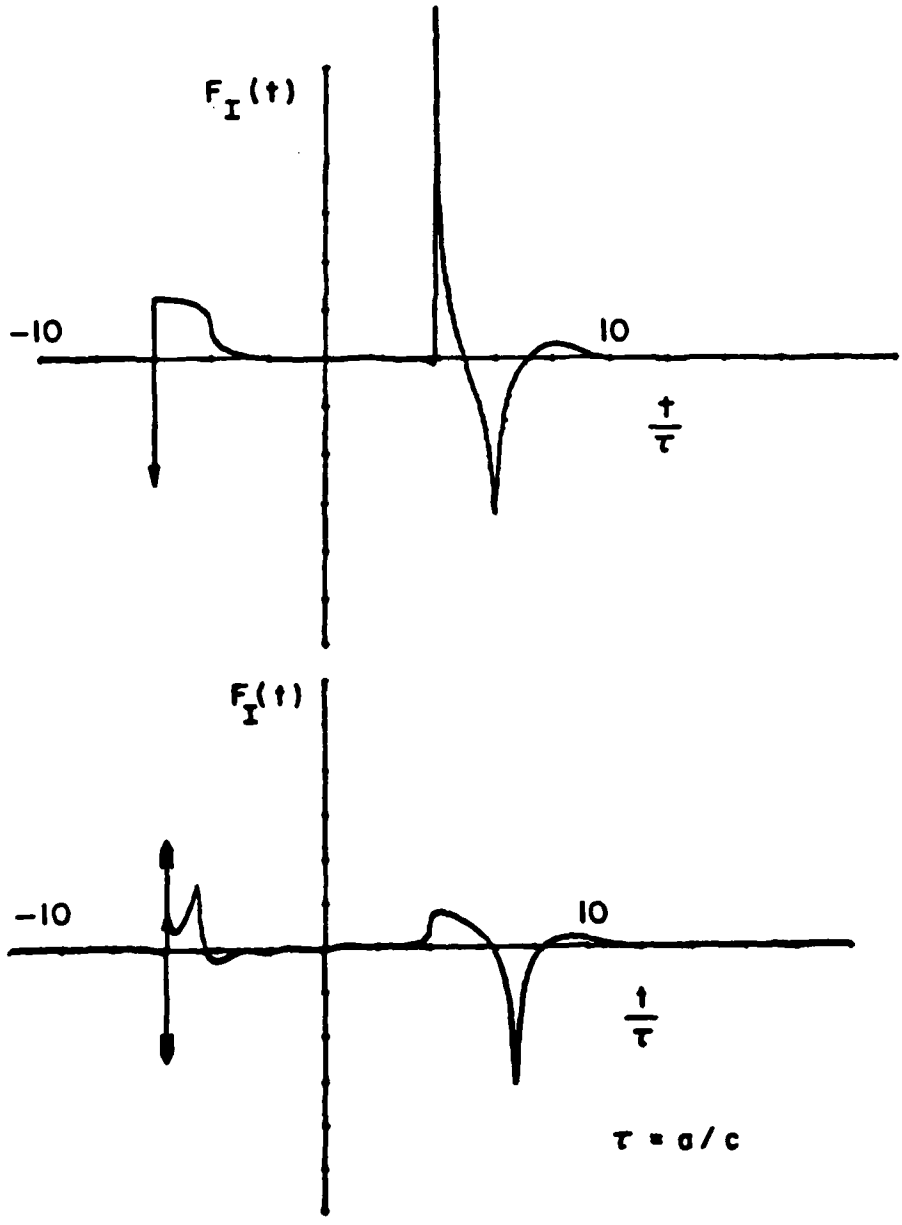

Figure 4-6. Theoretical impulse response approximation obtained via space-time integral equation technique [8] for a conducting 2:1 right circular cylinder with hemispherical cap on one end, at axial incidence. Bandwidth: $0 < ka < 30$.

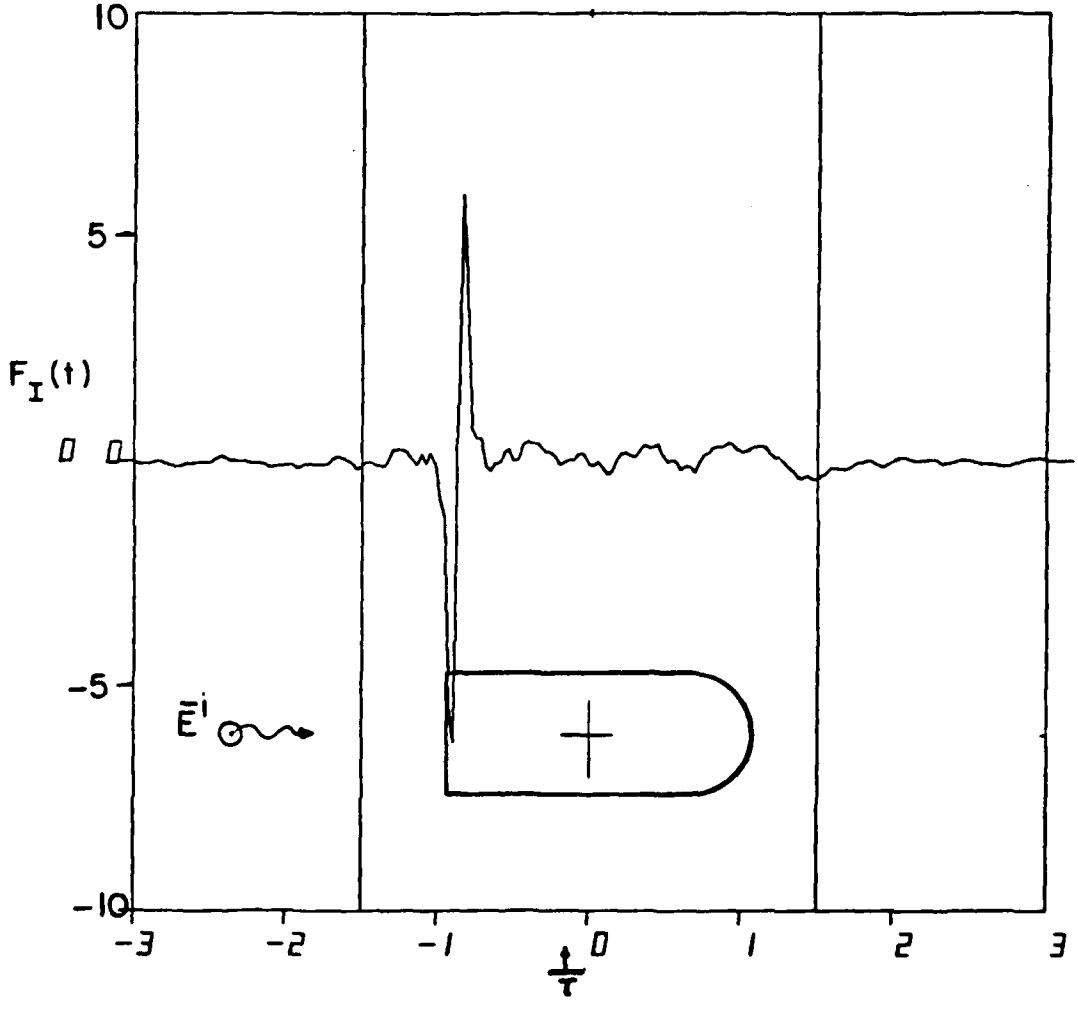

Figure 4-7. Measured impulse response of a conducting 2:1 right circular cylinder with hemispherical cap on one end. 180° case: axial incidence on the flat end. Time axis in units of $\tau = 5a/c$ where $L = 5a$ is the total length. Bandwidth: 960 harmonics for $1 \leq kL \leq 96$.

and the time shift theorem we find the inverse transform of F(s) given by

$$F_I(t) = \left(\frac{a}{c}\right)^2 \delta'(t) + \frac{1}{\pi}\left(\frac{a}{c}\right)^{\frac{1}{2}} \frac{1}{\sqrt{t - 2a/c}} \quad , \tag{4.11}$$

The first term is just the physical optics prediction. The second term suggests a resonant peak at $t = 2a/c$.

In [10] the exact Wiener-Hopf solution for scattering by an open circular waveguide in the resonance region is transformed into a time domain expression for the scattered electric field on axis given by

$$E^s(t) \sim \frac{-a}{2}\left[\delta(t) + \frac{1}{2\pi}\ \frac{c}{a}\left(-\frac{u(t - \frac{2a}{c})}{\sqrt{t - \frac{2a}{c}}} - \frac{u(\frac{2a}{c} - t)}{\sqrt{\frac{2a}{c} - t}}\right.\right.$$

$$\left.\left. - \frac{u(t - \frac{4a}{c})}{2\sqrt{2}\sqrt{t - \frac{4a}{c}}} + \frac{u(\frac{2a}{c} - t)}{2\sqrt{2}\sqrt{\frac{4a}{c} - t}} + \frac{u(t - \frac{6a}{c})}{3\sqrt{3}\sqrt{t - \frac{6a}{c}}} + \frac{u(\frac{6a}{c} - t)}{3\sqrt{3}\sqrt{\frac{6a}{c} - t}}\right)\right] . \tag{4.12}$$

Since the cylinder is open ended we would not expect the first term to be a doublet as it is for the flat end of the cylinder. But the second term, which has resonant peaks at multiples of $2a/c$, appears to be associated with multiple diffraction across the diameter. In Figure 4-8 the normalized time domain waveform is reproduced from [10]. The authors have noted that the ringing becomes negligible after the third peak. The same is true for the measured impulse response of Figure 4-7.

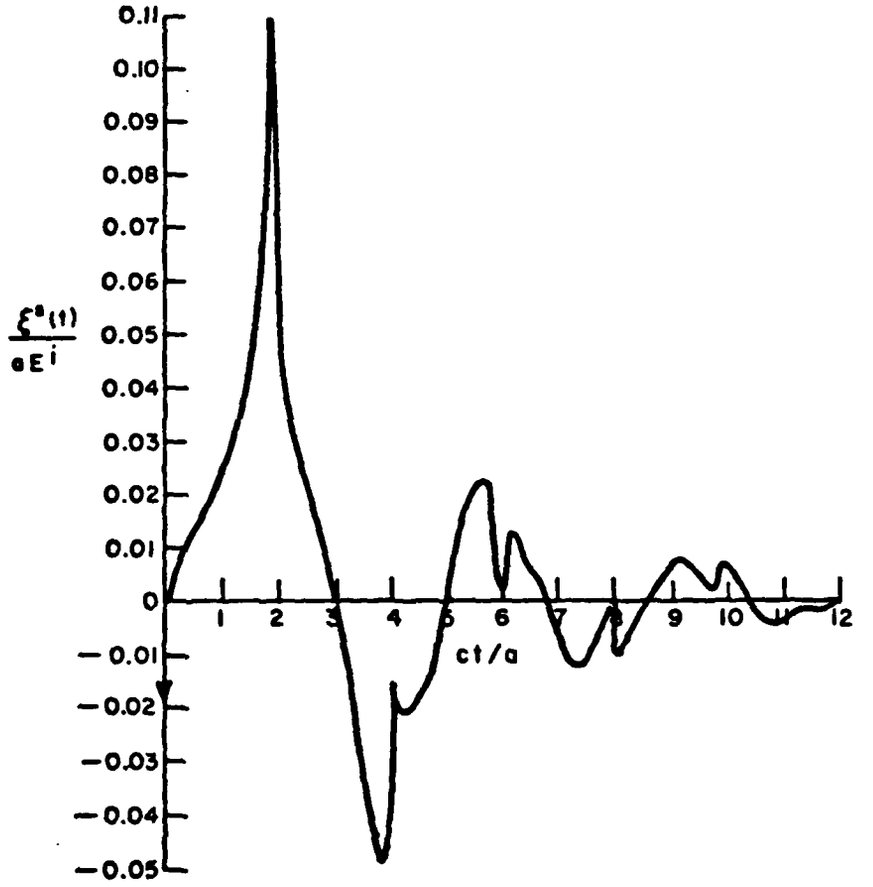

Figure 4-8. Inverse Fourier transform of "exact" Wiener-Hopf solution for field scattered by semi-infinite open circular waveguide at axial incidence [10]. Bandwidth: $0 < ka < 9.4$.

Finally, returning to the space-time integral equation approach, from [8] the impulse response for the sphere-capped cylinder with axial incidence on the flat end is shown in Figure 4-6b. Here the resonance is not as pronounced and does not continue through the creeping wave. Some of the ringing after the initial doublet can be seen, and the rounded positive swing preceeding the creeping wave is very similar to the corresponding portion of the measured impulse response.

So far we have compared measured time waveforms with several theoretical impulse responses. All are approximate in that they represent discrete Fourier transforms of bandlimited spectra. The measured spectra, in addition, are corrupted by noise which has been extracted to some extent by the methods described in Chapter III. The Gibb's phenomenon associated with truncation of the spectrum and other discontinuities has been treated to varying degrees in all the time waveforms. When viewing the measured waveforms it should be noted that the residual high frequency ripple may be further suppressed at the expense of time resolution.

For the sphere and for axial incidence on a body of revolution the backscattered radar cross section is independent of the polarization of the incident field. When the radar moves off axis the two polarization cases must be treated separately. The case of the incident electric field perpendicular to the plane formed by the direction of incidence and the axis of the scatterer is designated perpendicular (TE) polarization. The case of the incident electric field lying in that plnae is designated parallel (TM) polarization.

The measured impulse response for the sphere-capped cylinder at broadside (90°) is shown in Figure 4-9 for perpendicular (TE) polarization and Figure 4-10 for parallel (TM) polarization. The analysis splits most easily into two parts: behavior near the specular and behavior for late time. Near the specular the waveform should behave much like the physical optics approximation for the right circular cylinder without the spherical cap given in Figure 4-2b, where we noted a negative impulse and a positive singularity of order $(\frac{a}{c})^{3/2}$ $t^{-3}/2$. A consideration of the surface currents on the shadowed side of the cylinder [11] would lead us to expect physical optics to approximate the TM case more closely than the TE case. In the TM waveform of Figure 4-10 we see a negative impulse at the specular and a positive singularity less than half as high which drops rapidly to a positive constant value until a time corresponding to a distance of one cylinder diameter after the specular. This is the same overall shape seen in the physical optics approximation.

A first order Uniform Theory of Diffraction solution for the sphere-capped cylinder [12] has been inversed Fourier transformed to produce the impulse response approximation in Figure 4-11. The geometry for the first order UTD solution is shown in Figure A-4 for the various angles of incidence. The first order solution includes the contribution from the edge at the flat end of the cylinder and the discontinuity in surface curvature at the junction of the spherical cap. At aspects off broadside a third contribution comes from either the reflected specular on the sphere or the rear edge of the flat end rim depending upon which

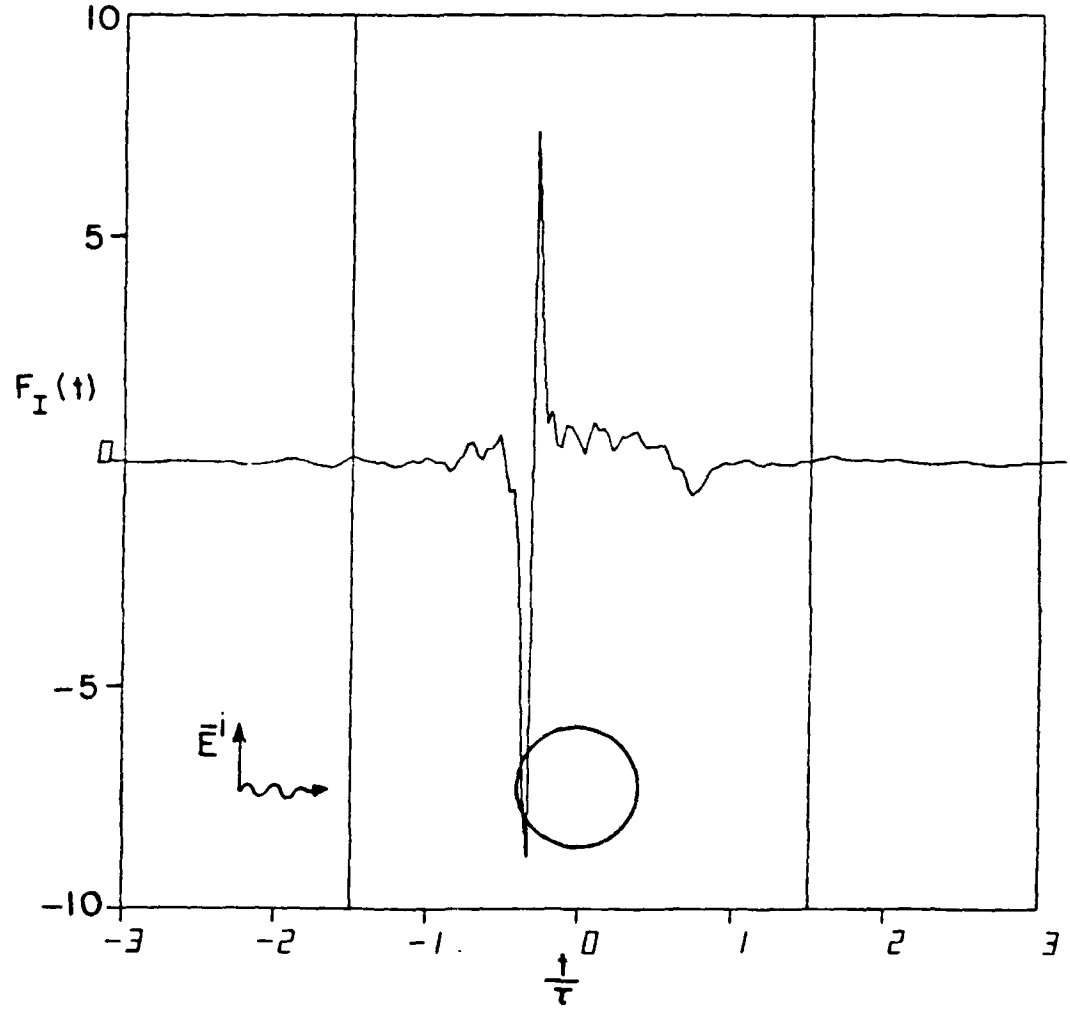

Figure 4-9. Measured impulse response of a conducting 2:1 right circular cylinder with hemispherical cap on one end.
90° case: broadside.
Perpendicular polarization (TE).
Time axis in units of $\tau = 5a/c$ where L=5a is the total length.
Bandwidth: 960 harmonics for $1 < kL < 96$.

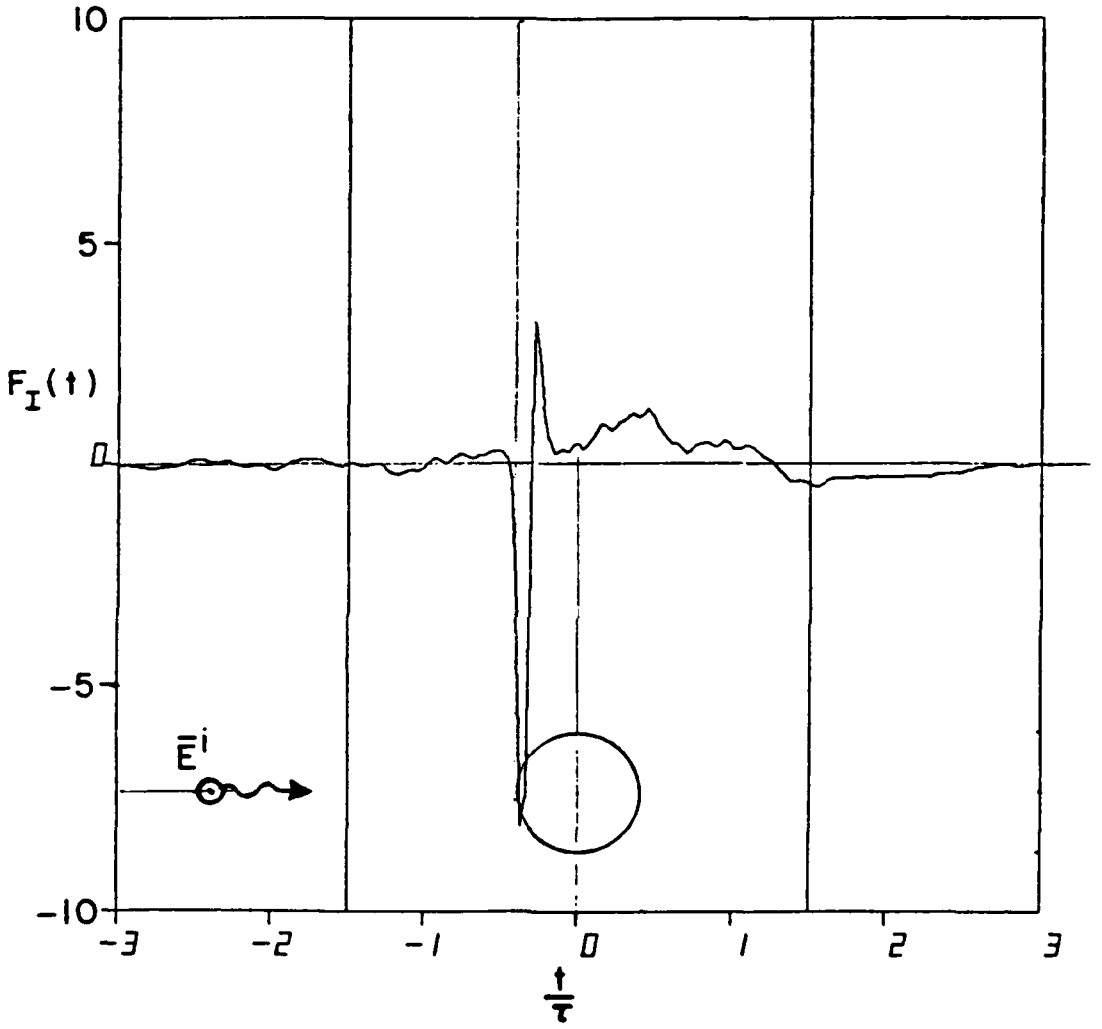

Figure 4-10. Measured impulse response of a conducting 2:1 right circular cylinder with hemispherical cap on one end.
90° case: broadside.
Parallel polarization (TM).
Time axis in units of $\tau = 5a/c$ where L=5a is the total length.
Bandwidth: 960 harmonics for $1 < kL < 96$.

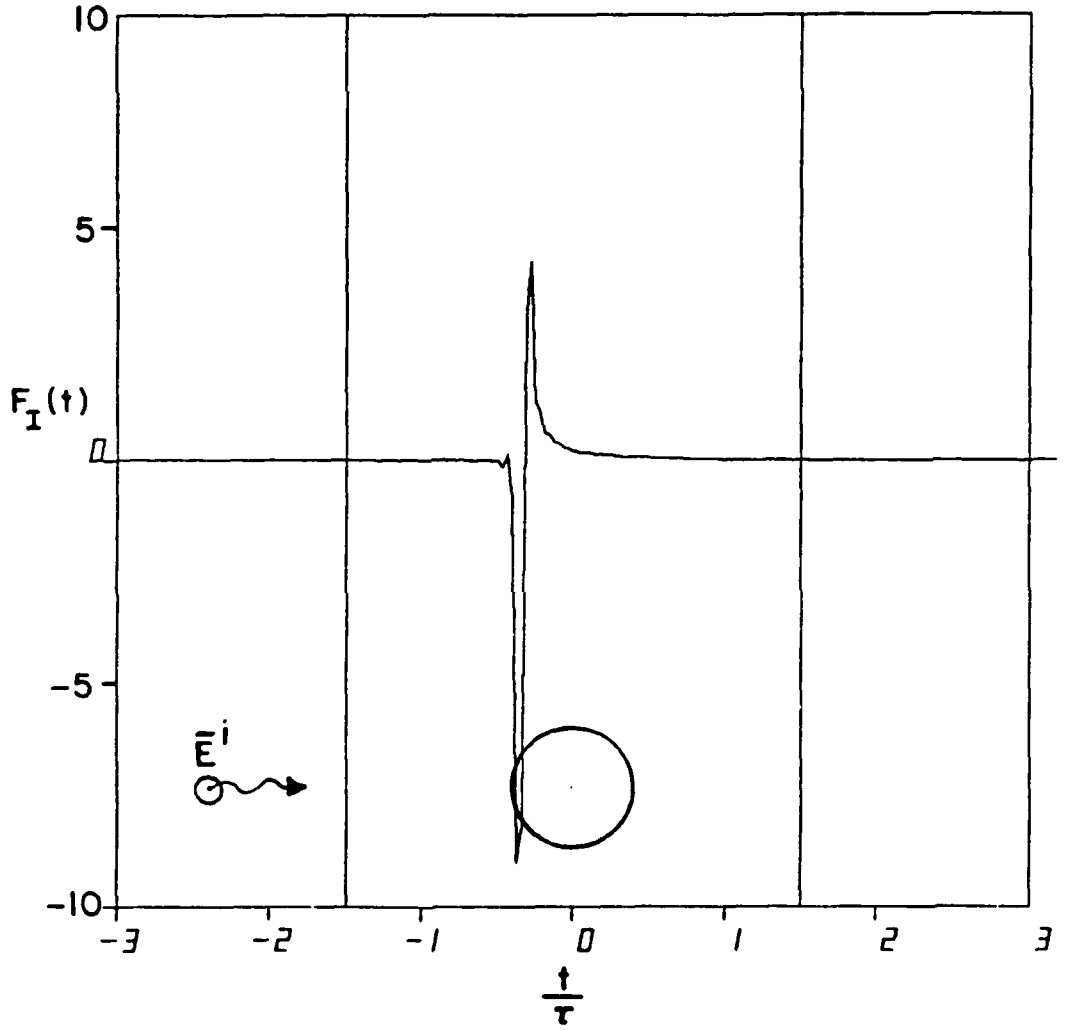

Figure 4-11. First order UTD impulse response of a conducting 2:1 right circular cylinder with hemispherical cap on one end.
90° case: broadside.
Parallel polarization (TM)$_z$
Time axis in units of $\tau = 5a/c$ where L=5a is the total length.
Bandwidth: 960 harmonics for $2 < kL < 96$.

lies in the lit region. A thorough discussion of the UTD solution is found in [12]. In the symmetrical case of the cylinder with spherical caps on both ends the transfer function for the scattered field at broadside simplifies to

$$F(jw) = -\frac{a}{c} + \frac{2}{\sqrt{\pi}} \left(\frac{a}{c}\right)^{3/2} \sqrt{j\omega} \quad . \tag{4.13}$$

We can see that the first term gives the inverse transform $-\left(\frac{a}{c}\right) \delta(t)$, which is the specular from a sphere. The term involving $\sqrt{j\omega}$, associated with the cylindrical curvature, does not have a well defined inverse Laplace transform in analytic form because of a singularity of order $t^{-3}/2$. But this is exactly the behavior we have noted previously for times immediately following the specular return.

Because of the high quality of the UTD spectrum the amplitude of the UTD impulse response in Figure 4-11 has been reduced to 3/4 scale. Allowing for this scale factor the measured TM impulse response compares extremely well with the UTD waveform.

Continuing the early time analysis, let us consider the measured TE impulse response in Figure 4-9. The negative impulse for this polarization is nearly identical to that of the TM case. But the positive singularity has significantly greater amplitude and drops to a positive step level much higher than the TM waveform. To understand this behavior, refer to [7] in which the impulse response of a right circular cylinder is derived from a normalization of the Keller GTD solution for the infinite cylinder [13]. The results, shown in Figure 4-13, give a sign difference between the two polarizations in the jump

discontinuity after the specular. The difference is based on the sign difference in the second term of the Luneberg-Kline expansion for the reflected field. This term, involving powers of $1/j\omega$, is a higher order term which is not included in the first order UTD solution. Its inverse transform is a unit step, $u(t)$. For the infinite cylinder the reflected field is the only contribution to the scattered field except for possible creeping waves which would appear later in time. But when the cylinder is finite the end contributions, which we have seen to be of order $\sqrt{j\omega}$ dominate the $1/j\omega$ term. It is just this $1/j\omega$ term which accounts for the difference between the two measured impulse responses at the jump discontinuity immediately after the specular return.

The conclusions to be drawn at this point are twofold. First, the measurements have recovered a higher order effect. Secondly, while the first order UTD solution converges at broadside to the same results for the TE and TM cases, a UTD solution whch includes the higher order term is quite capable of predicting the slight difference between the two polarizations.

The late time analysis will begin with the measured TM impulse response in Figure 4-10. The waveform reaches a relative null at a time corresponding to approximately one half the total object length. At this point a low frequency whole-body resonance begins which dominates the remainder of the waveform. The first peak of this resonance is at approximately $4/5\tau$ after the specular and the resonant period is slightly less than 0.7τ. A complete solution for the scattered field from a cylindrical structure with length to diameter ratio on the order

of 2:1 is not yet available in the resonance region. But as a rough approximation the sphere-capped cylinder may be modeled as a short fat dipole. Calculations of the radar cross section of cylindrical antennas are given in [14] as a function of frequency and length to radius ratio (See also [15]). While these results are given only for length to radius ratios as low as L/a = 45 (compared to L/a = 5 for the sphere-capped cylinder) the general trend indicates a second resonant peak at kL = 3π which becomes much stronger for decreasing L/a ratios. As can be seen in Figure 4-10, the measured waveform resonates with a period $T_2 = 0.7\tau$, or kL = 2.9π.

The entire TM waveform appears to be superimposed upon a sinusoid of period, T_1, equal to approximately 3τ, corresponding to kL = $\frac{2}{3}\pi$. While the first resonant peak for a thin dipole occurs at kL=π (or L = $\lambda/2$) it is noted in [14] that this peak shifts noticeably toward lower values of kL as the length to radius ratio decreases. This is consistent with the period, T_1, noted above. Thus the measured TM waveform shows evidence of two natural resonances of the sphere-capped cylinder.

By means of comparison the measured TM impulse response of a 2:1 right circular cylinder without the spherical cap is shown in Figure 4-12. All the characteristics of the TM sphere-capped cylinder waveform are again evident in Figure 4-12, except that the natural resonance appears to be not quite as strong. We would expect this to be the case since the spherical cap decreases the influence of the radial currents across the ends of the cylinder. For this same reason the dipole model

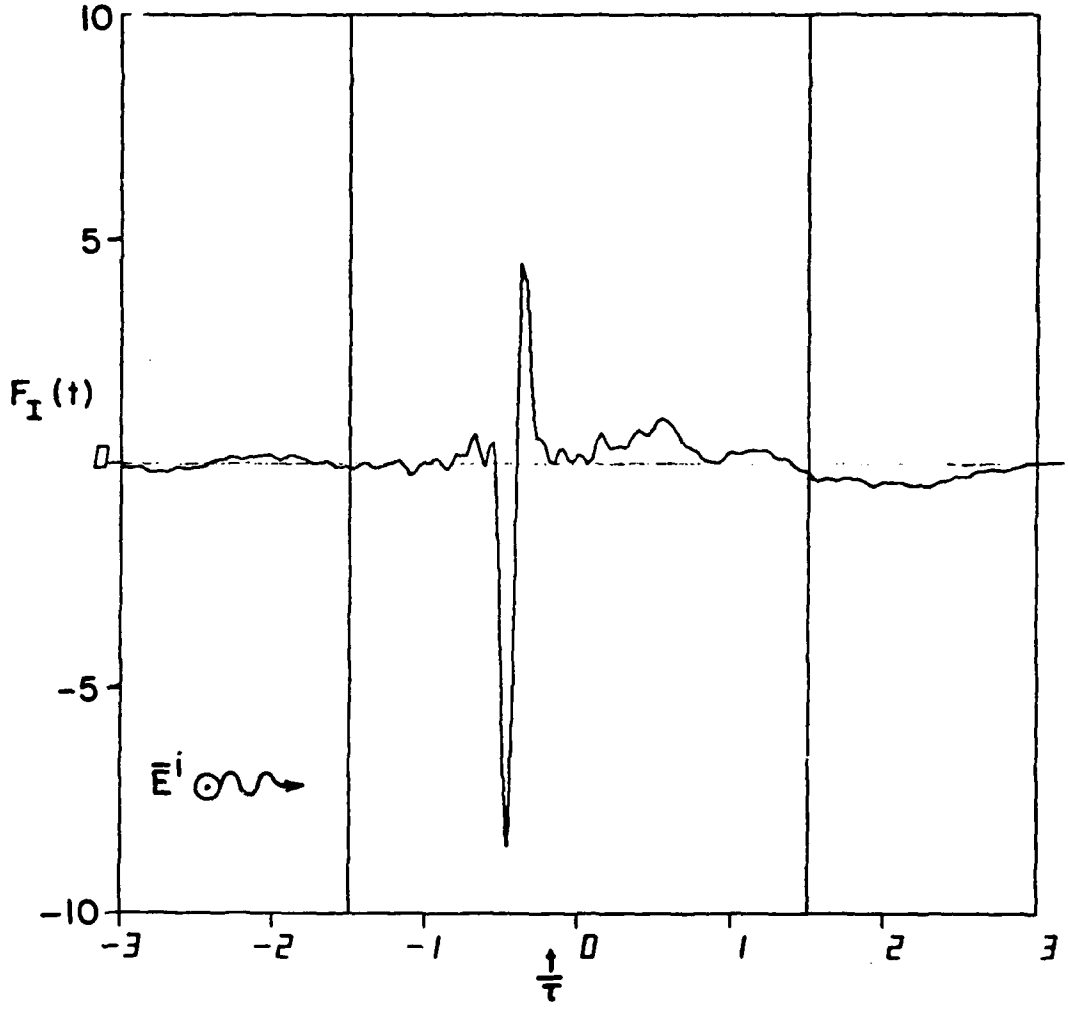

Figure 4-12. Measured impulse response of a conducting 2:1 right circular cylinder.
90° case: broadside.
Parallel polarization (TM).
Time axis in units of $\tau = 4a/c$ where L=4a is the total length.
Bandwidth: 766 harmonics for $0.8 < kL < 76$.

more closely approximates the sphere-capped cylinder than the flat end cylinder [16].

The late time behavior of the measured TE impulse response of the sphere-capped cylinder in Figure 4-9 has a positive step and a creeping wave. The creeping wave around the cylinder appears in Figure 4-13, which is reproduced from [7]. In Figure 4-13 the specular term has been removed and the polarity of the perpendicular (TE) waveform reversed. With the specular term removed it can be seen that the second term of the Luneberg-Kline expansion is responsible for the step behavior. In both Figures 4-9 and 4-13 the transition from the positive step into the creeping wave appears more abrupt for the cylindrical surface than for the sphere, due to the fact that the creeping wave paths do not cross a caustic.

Superimposed upon the step portion of the measured waveform of Figure 4-9 is a pronounced ringing. In light of the amount of precursor in this particular waveform it appears that the ringing is measurement error. In this connection the measured TE impulse response for the right circular cylinder without the spherical end cap is shown in Figure 4-14. The aforementioned ringing is noticeably absent. All other features describes for the sphere-capped cylinder are in evidence. Note in particular the rapid transition into the creeping wave.

When the sphere-capped cylinder is rotated to a 45° look angle the scattering phenomena become slightly more complicated. The measured TM impulse response at 45° is shown in Figure 4-15 along with the

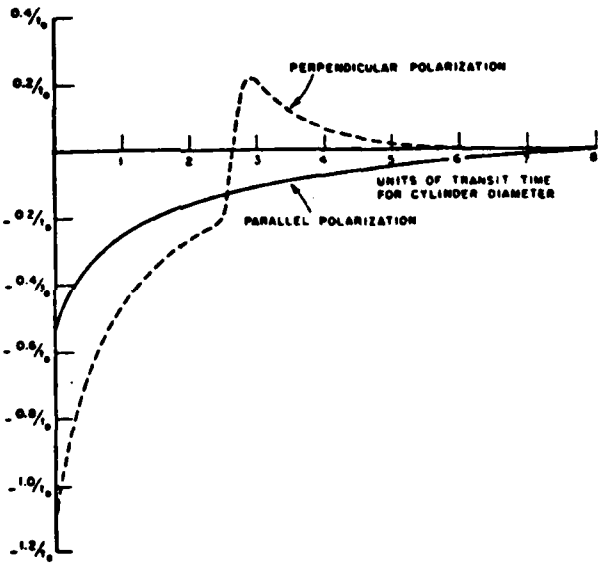

Figure 4-13. GTD impulse response of a conducting right circular cylinder (reproduced from [7]).
Specular term removed.
90° case: broadside.
Polarity of perpendicular polarization waveform reversed.
Time axis in units of $\tau = 2a/c$ where a = cylinder radius.
Bandwidth: 79 harmonics for $0.157 < ka < 12.4$.

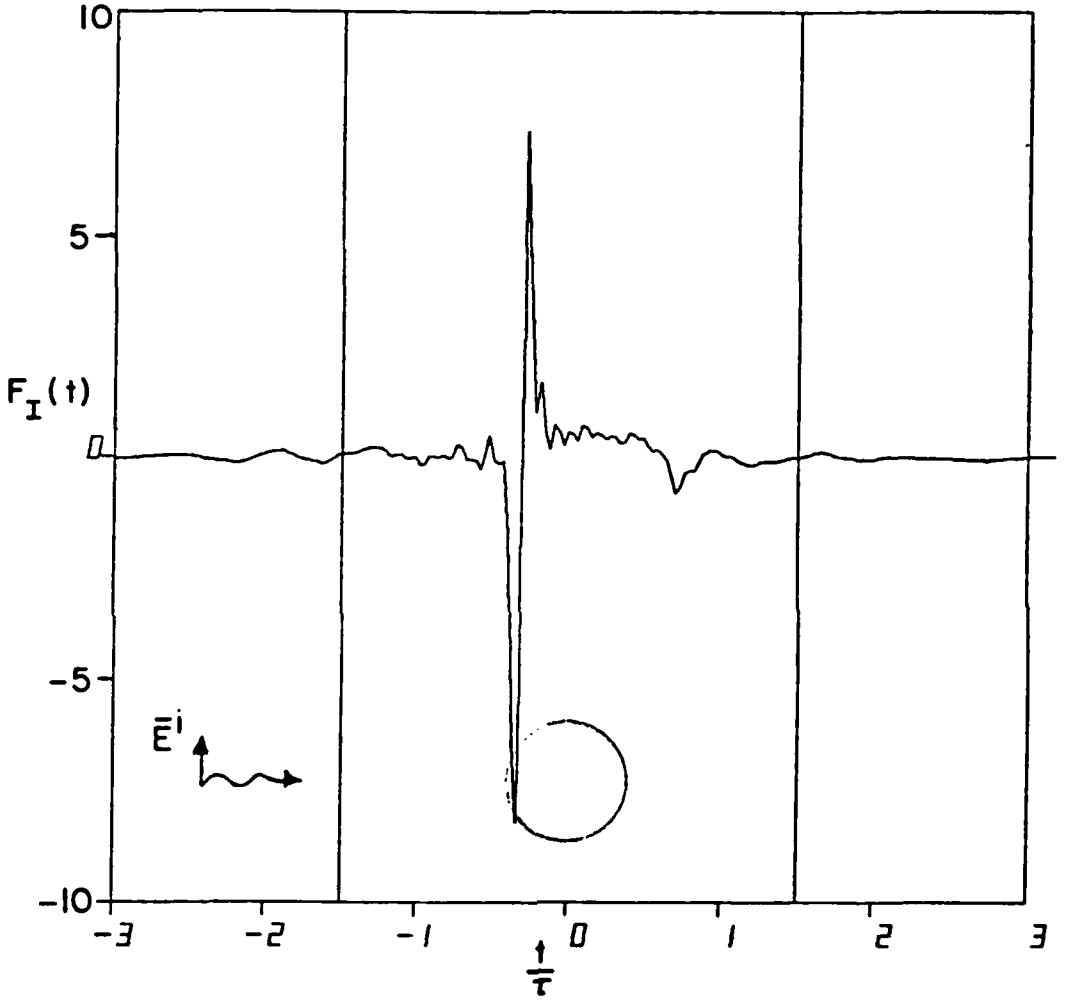

Figure 4-14. Measured impulse response of a conducting 2:1 right circular cylinder.
90° case: broadside.
Perpendicular polarization (TE).
Time axis in units of $\tau = 4a/c$ where L=4a is the total length.
Bandwidth: 766 harmonics for $0.8 < kL < 76$.

corresponding first order UTD impulse response. The TE case is shown in Figure 4-16. Note that the measured TM impulse response covers a smaller bandwidth (1.0 < kL < 64.) than the TE case. In order to obtain a fair comparison the UTD solution is restricted to the same bandwidth. Again the analysis is split into times near the specular and late times.

The specular return is identical for both polarizations and for UTD versus measured waveforms, indicating the specular term is polarization independent. Immediately after the specular both measured waveforms begin a positive step just as in the case of the sphere or sphere-capped cylinder at 0°. This step behavior is not seen in the first order UTD waveform indicating the absence of the 1/k term from the Luneberg-Kline expansion, as discussed in connection with the broadside cylinder.

When the incident field reaches the junction between the sphere and cylinder we see a noticeable difference in the response of the two polarizations to the discontinuity in surface curvature at the junction. As a heuristic explanation consider that in the TE case the radius of curvature, a , in the direction parallel to the incident electric field vector does not change across the junction between sphere and cylinder. The TE waveform responds relatively slowly and continuously to the discontinuity in surface curvature. In the TM case the radius of curvature in the direction parallel to the incident electric field vector jumps from a to infinity across the junction. In the measured TM waveform the response drops abrubtly to zero at the junction indicating

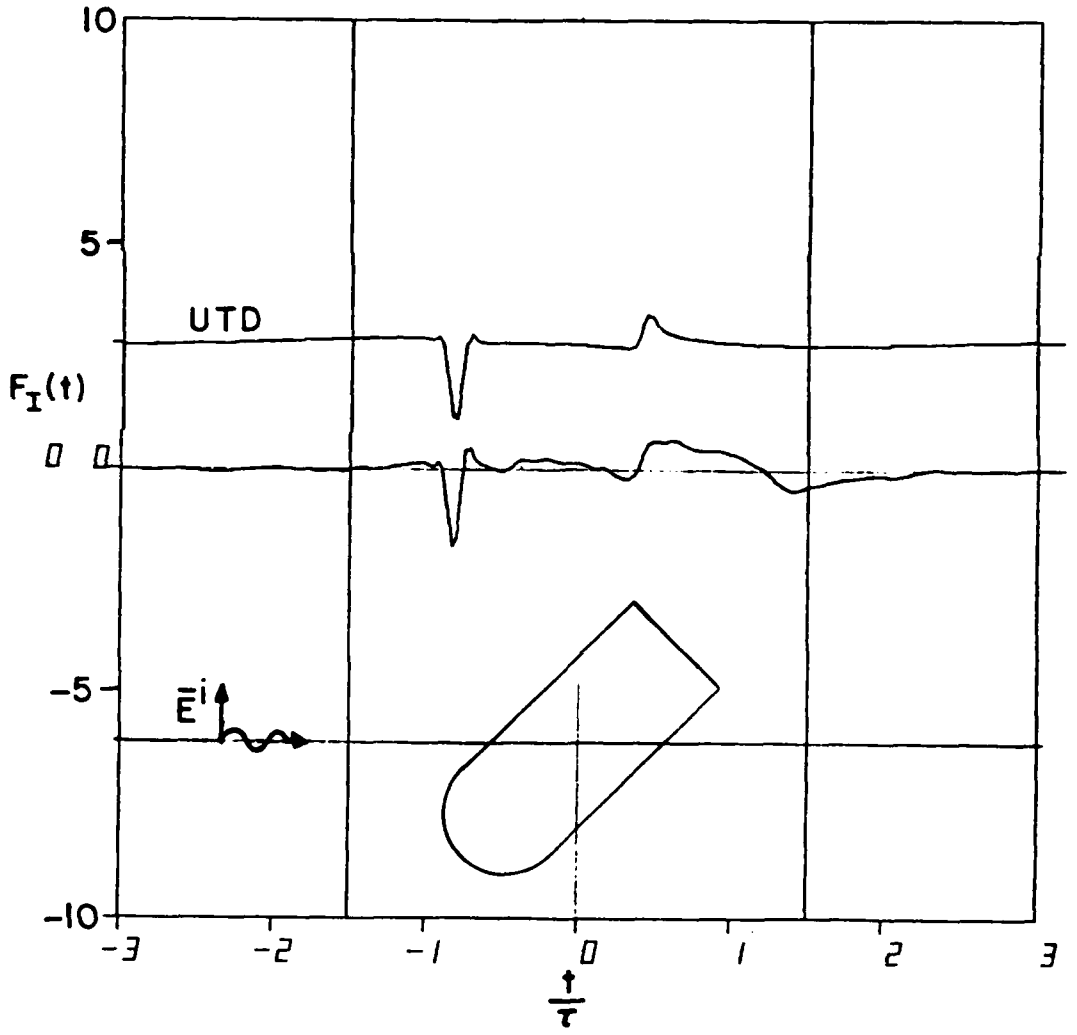

Figure 4-15. Measured versus first order UTD impulse response of a conducting 2:1 right circular cylinder with hemispherical cap on one end.
45° case.
Parallel polarization (TM).
Time axis in units of $\tau = 5a/c$ where L=5a is the total length.
Bandwidth: 640 harmonics for $1 < kL < 64$.

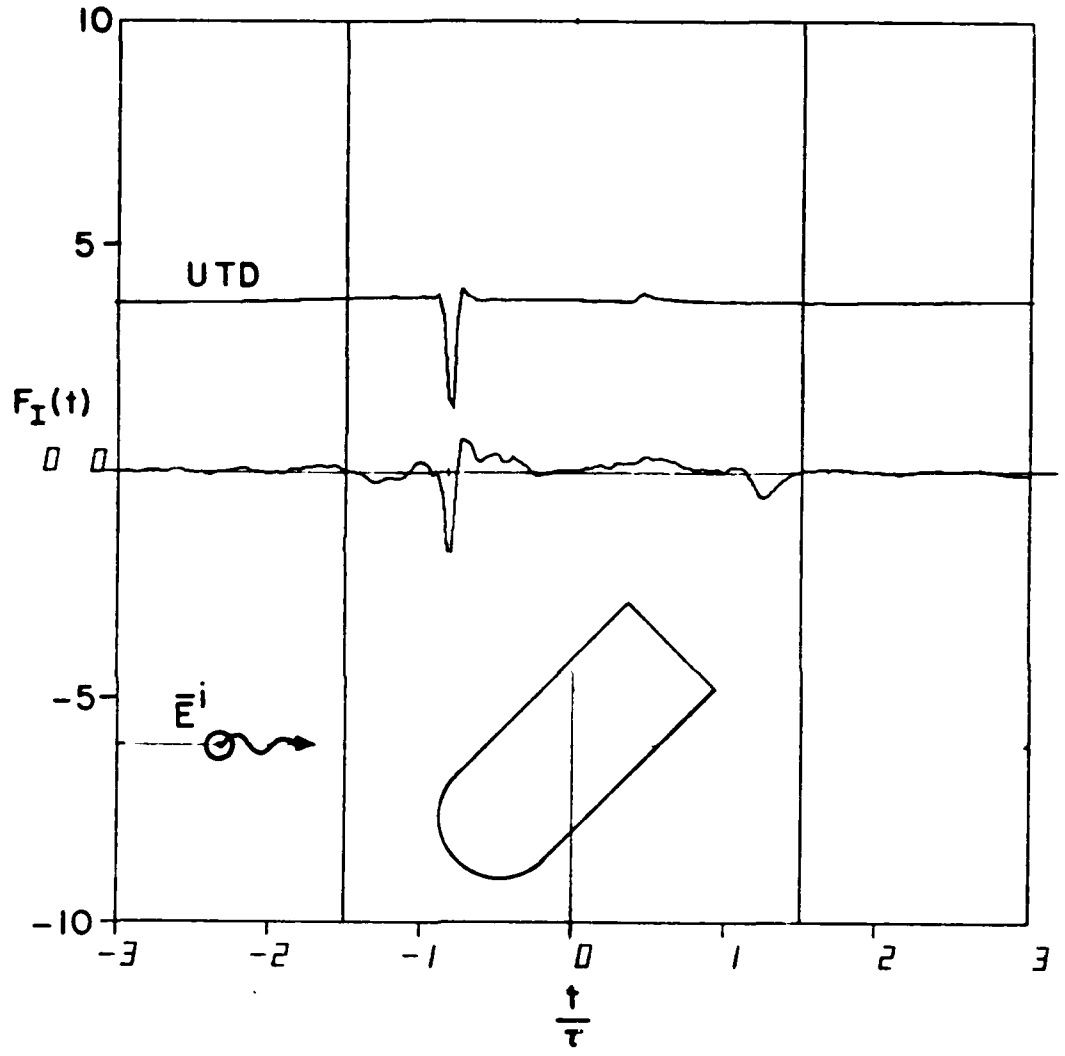

Figure 4-16. Measured versus first order UTD impulse response of a conducting 2:1 right circular cylinder with hemispherical cap on one end.
45° case.
Perpendicular polarization (TE).
Time axis in units of $\tau = 5a/c$ where L=5a is the total length.
Bandwidth: 960 harmonics for $1 < kL < 96$.

the impulse response is polarization sensitive to the discontinuity in surface curvature.

The late time behavior shows significant differences between the two polarizations associated with diffraction from the rear edge of the cylinder. We will begin the late time analysis with the TE case. The UTD waveform shows a weak positive return from the point of the rear cylinder rim nearest the radar. This small spike appears as the high point in the center of a wide, shallow positive swing in the measured waveform. The mechanism responsible appears to be a low frequency effect outside the regime of UTD and localized scattering.

The distinctive late time feature in the measured TE waveform is a wide negative excursion centered at a time 2τ after the specular. It has the time dispersion and cusp shape characteristic of a creeping wave. A plausible explanation for this scattering mechanism may be proposed using a UTD argument involving a spiral creeping wave path and diffraction from the rear edge. Figure 4-17 shows the geometry for the possible ray paths. The incident shadow boundary lies along the top of the cylinder parallel to the axis. A continuum of rays may attach at this shadow boundary and creep along a spiral path to the rear cylinder edge. Each ray diffracts from the edge and creeps back along a symmetric spiral path on the other side of the cylinder to launch in a backscatter direction at the opposite shadow boundary. If the cylinder is "unwrapped" from shadow boundary to shadow boundary it can be shown by simple geometry that the same total distance is travelled by each of these rays. The path length referenced to the specular point is ℓ =

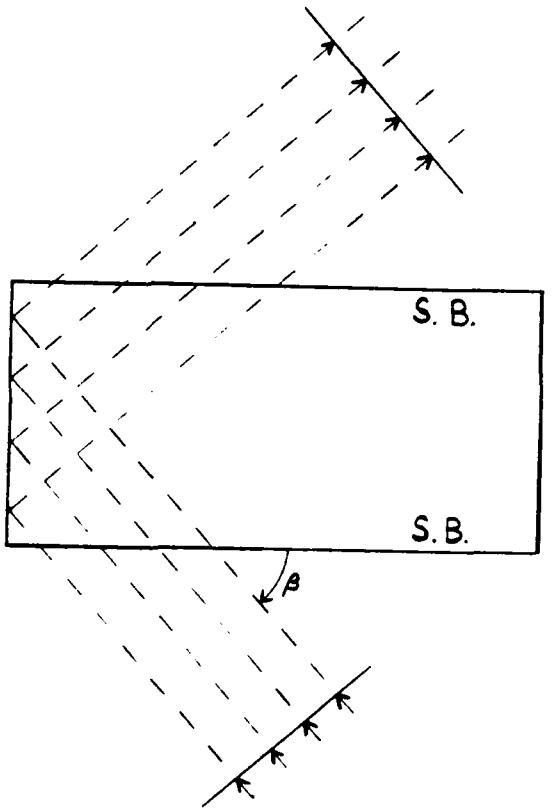

Figure 4-17. Ray paths for creeping wave and diffraction from rear cylinder edge.

$2a[1+2\sqrt{2} + \pi/2\sqrt{2}] = 9.88a$. Thus we would expect the peak of the creeping wave to occur at a time $t_{cw} = 1.98\tau$ after the specular. Due to the phase factor $e^{-jkt_{cw}-j\alpha(w^{1/3})t}$ discussed earlier in connection with creeping waves [17], we expect this feature to be dispersed in time. The difference between the expected time of arrival of this proposed mechanism and the time read off the measured waveform is less than 1 percent. Such a comparison is very convincing evidence that the proposed mechanism accounts for the measured phenomenon.

The foregoing discussion may serve to demonstrate the utility of the impulse response waveform in understanding specific scattering mechanisms and improving the accuracy of theoretical formulations. The expected arrival time of the response from a specific scattering center is obtained from exactly the same calculation as the phase factor associated with each diffraction coefficient in a UTD analysis. Therefore a logical and convenient place to verify the UTD results is on the time axis. Since UTD is a superposition of distinct, local scattering mechanisms the impulse response displays their relation to the geometry of the scatterer quite naturally.

The late time behavior of the TM waveform presents an equally intriguing problem. At the leading edge of the rear cylinder rim both the UTD and measured waveforms show a strong positive spike. This point is the stationary point for first order diffraction from the entire rear rim of the cylinder. The measured waveform shows this single diffraction mechanism at the leading edge of a wide positive excursion.

The position, height, and rise time of this feature is nearly identical to that of the UTD waveform. But after peaking at the leading edge of the rear rim the measured TM waveform tapers slowly and continuously to zero after a time of approximately 0.7τ and remains negative for another τ seconds.

The measured waveform suggests that a ring current is induced on the cylinder rim. Such a mechanism could be treated with an equivalent currents approach [9]. As a step toward understanding the phenomenon the UTD impulse response has been subtracted from the measured TM impulse response. The difference waveform is shown in Figure 4-18 along with the UTD, measured, and difference spectra. The spectrum of the difference shows significant energy in both the low and high frequency regions. In addition, the difference spectrum shows a fairly even periodicity at intervals of kL = 5 corresponding to a fundamental frequency of $\omega_0 = 5/\tau$. It can be seen that this resonance does not correspond to a period evident in either the measured or UTD spectrum. If we related the interference to a path length, ℓ, corresponding to some physical dimension of the scatter we would get nulls at intervals of $e^{-jk\ell} = e^{-jn\pi}$. Using the value of ω_0 we obtain $\ell = n\pi a$ or half the circumference of the cylinder rim. It would seem logical to expect the resulting time response to change polarity at n = 1 corresponding to a time $\frac{\pi}{5}\tau = 0.63\tau$ after the leading edge of the rear rim. This is the approximate time of the zero crossing in the measured waveform.

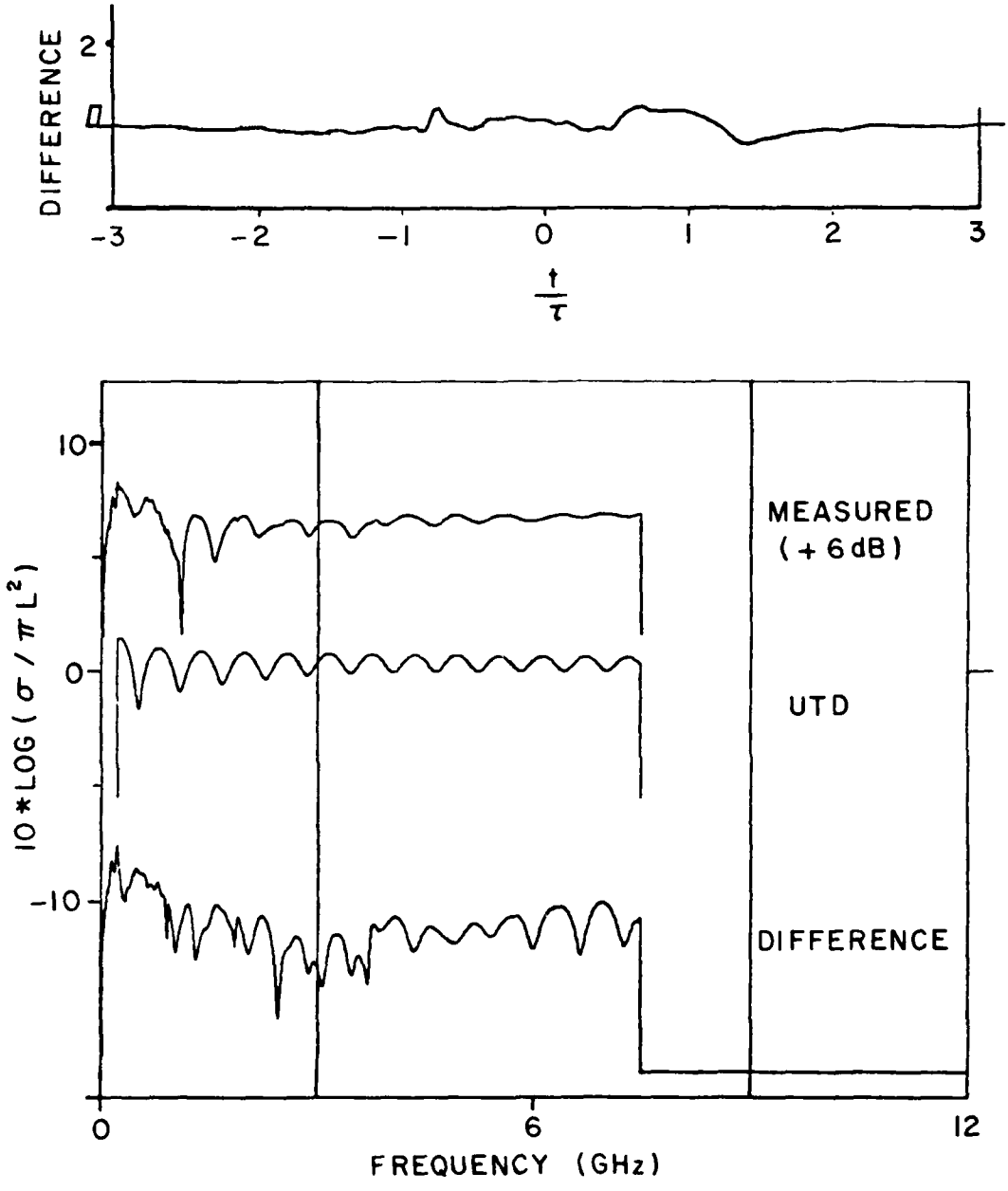

Figure 4-18. (a) Time waveform of difference between measured and first order UTD impulse responses for sphere-capped cylinder at 45°; TM.

(b) UTD, measured, and difference spectra of sphere-capped cylinder at 45°; TM.

The above discussion is somewhat heuristic and is not meant to provide the definitive explanation for the observed behavior but is intended to illustrate the possible uses of the impulse response waveform in scattering analysis.

Finally the sphere-capped cylinder is rotated to 135°. At this look angle we do not have a reflected field specular as in the previous cases. The TM impulse response is presented in Figure 4-19 and the TE in Figure 4-20. We will begin the early time analysis with the TM waveform.

In Figure 4-19 we see an excellent correlation between the measured and UTD waveforms at the front cylinder disc. The response is very similar to the tangent curve obtained from the physical optics approximation for the disc away from normal incidence (Figure B-3). For this polarization the response is symmetric from both leading and trailing edges of the disc. We have already seen that as the angle of incidence rotates to normal the response converges to a doublet.

For TE polarization in Figure 4-20 we do not see the same symmetry. The response from the leading edge is strong and that from the trailing edge much weaker. Again the UTD and measured waveforms compare very well. Note that just as in the broadside cylinder case the physical optics approximation provides a better prediction of the TM behavior. We may safely say that the early time response is sensitive to polarization.

While the early time response characterizes the sphere-capped cylinder for this look angle the late time response shows some more

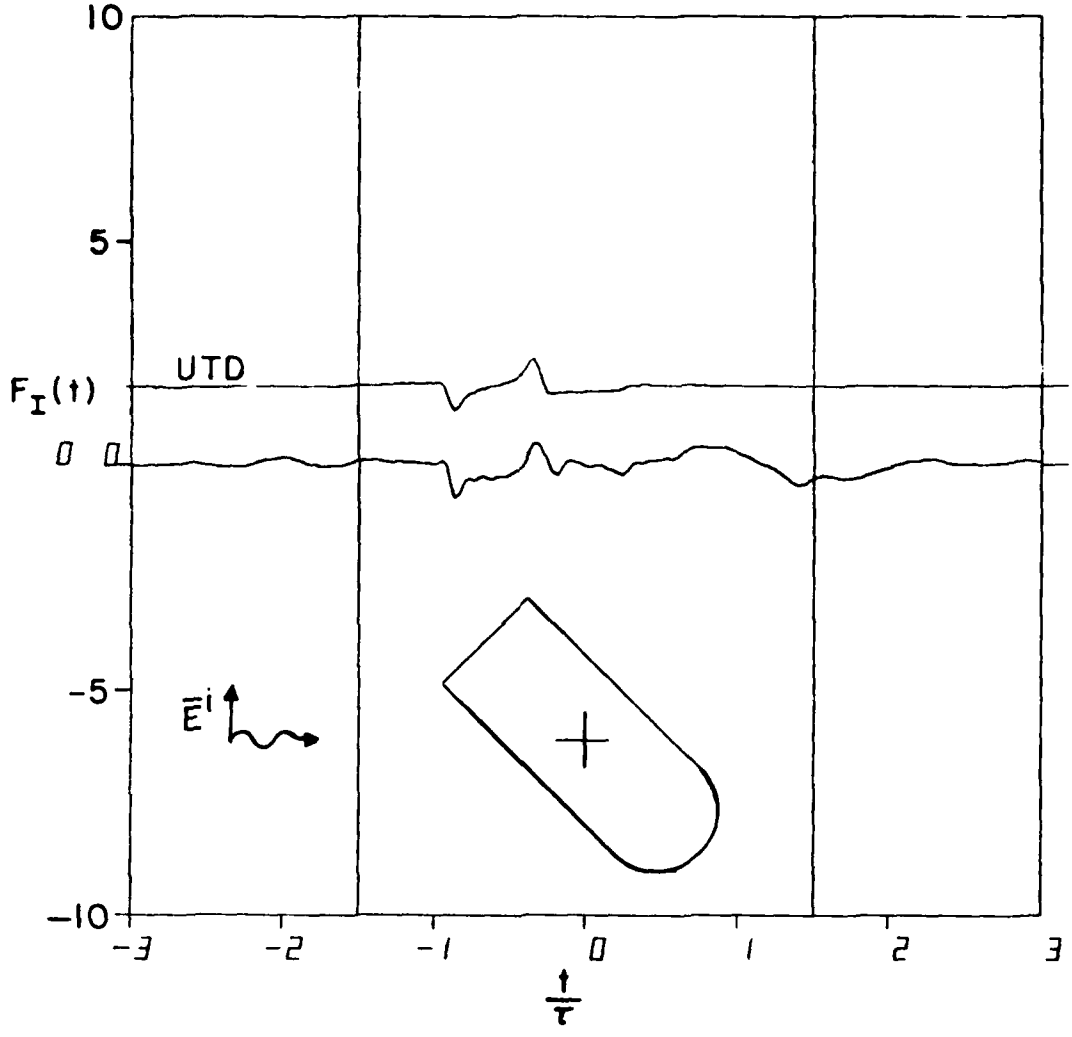

Figure 4-19. Measured versus first order UTD impulse response of a conducting 2:1 right circular cylinder with hemispherical cap on one end.
135° case.
Parallel polarization (TM).
Time axis in units of $\tau = 5a/c$ where L=5a is the total length.
Bandwidth: 640 harmonics for $1 < kL < 64$.

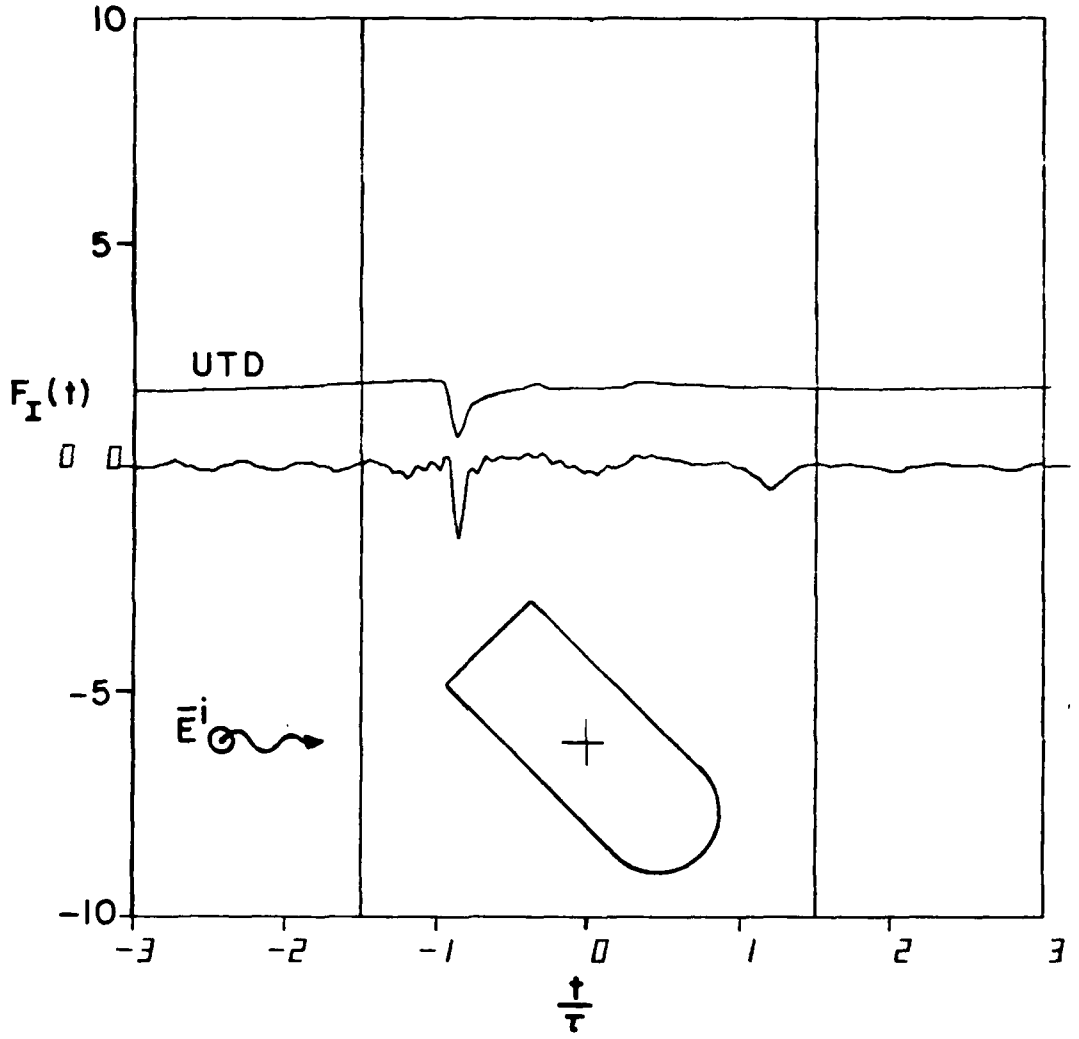

Figure 4-20. Measured versus first order UTD impulse response of a conducting 2:1 right circular cylinder with hemispherical cap on one end.
135° case.
Perpendicular polarization (TE).
Time axis in units of $\tau = 5a/c$ where L=5a is the total length.
Bandwidth: 640 harmonics for $1 \leq kL \leq 64$.

subtle features. We do not see any of the resonance associated with the disc diameter as we saw in the 180° case. But the TM waveform shows a low frequency ringing with a period of approximately 0.9τ. We would expect a weaker version of the dipole resonance noted in the broadside case, where the period of 0.7τ agreed with theoretical results. The nature of such ringing for aspects off broadside is not obvious.

In the TM waveform we see a creeping wave which attaches on the spherical cap, creeps around the sphere, skirts the cylinder wall, and diffracts from the cylinder edge furthest from the radar. From the geometry we can calculate the arrival time of this creeping wave as $t_{cw} = 1.4\tau$. This time corresponds to the lowest point on the late time TM waveform. The cusp shape is apparent even though it appears superimposed upon the low frequency sinusoid noted earlier. Although the magnitude of this creeping wave is decreased by the edge diffraction it is still seen to be a measurable contribution.

The distinctive feature in the late time TE waveform is the creeping wave which attaches at the sphere-cylinder junction, creeps around the sphere, and launches from the point on the junction diametrically opposite. It is seen at $t_{cw} = 1.1\tau$ in Figure 4-20. Its shape and magnitude indicates that it is unaffected by the presence of the cylinder. For both polarizations it is a simple matter to include the creeping wave term in the UTD solution.

The preceeding discussion has covered five major look angles and two principal polarizations. The sphere-capped cylinder is seen to represent several types of specular behavior, multiple interactions, and

low frequency resonance. Specific scattering mechanisms may be verified by rotating the object slightly and examining the resultant time shift, or absence of it, in the impulse response. Multiple interactions between the sphere and cylinder fall out when the sphere-capped cylinder waveform is compared to that of the cylinder without the spherical cap. And by subtracting known UTD terms from the measured waveforms we find out which additional scattering mechanisms are significant. These and other mechanisms may be examined further by considering the cross polarized impulse response. All of these methods are made possible by the unique relation between the impulse response waveform and the scattering geometry.

CHAPTER V

CROSS-POLARIZED MEASUREMENTS

In order to measure cross-polarized backscatter, it was necessary to select a suitable calibration target to replace the sphere, which has no cross-polarized return. A calibration target must satisfy the following criteria: 1) it must be broadband, i.e., not highly resonant; 2) it must have a known, readily available exact solution; and 3) it must be relatively insensitive to positioning. The geometry for the cross-polarized measurements is sketched in Figure 5-1. A narrow, thin strip at edge-on incidence was chosen as a calibration target. At edge-on, the thin strip was known to satify the third criterion as shown in Figure 5-2 [21]. It was predicted and proven that a narrow strip would be broadband. And, finally, a moment method solution was available.

At a tilt of 45° off vertical, the edge-on strip gives a cross-polarized return comparable in magnitude to the co-polarized return of the calibration spheres. The strip has a cosine sensitivity to error in the amount of tilt. Co-polarized measurements of the edge-on strip calibrated against a sphere, shown in Figure 5-3, verify that the narrow ($< \lambda/4$) strip is indeed broadband in both amplitude and phase.

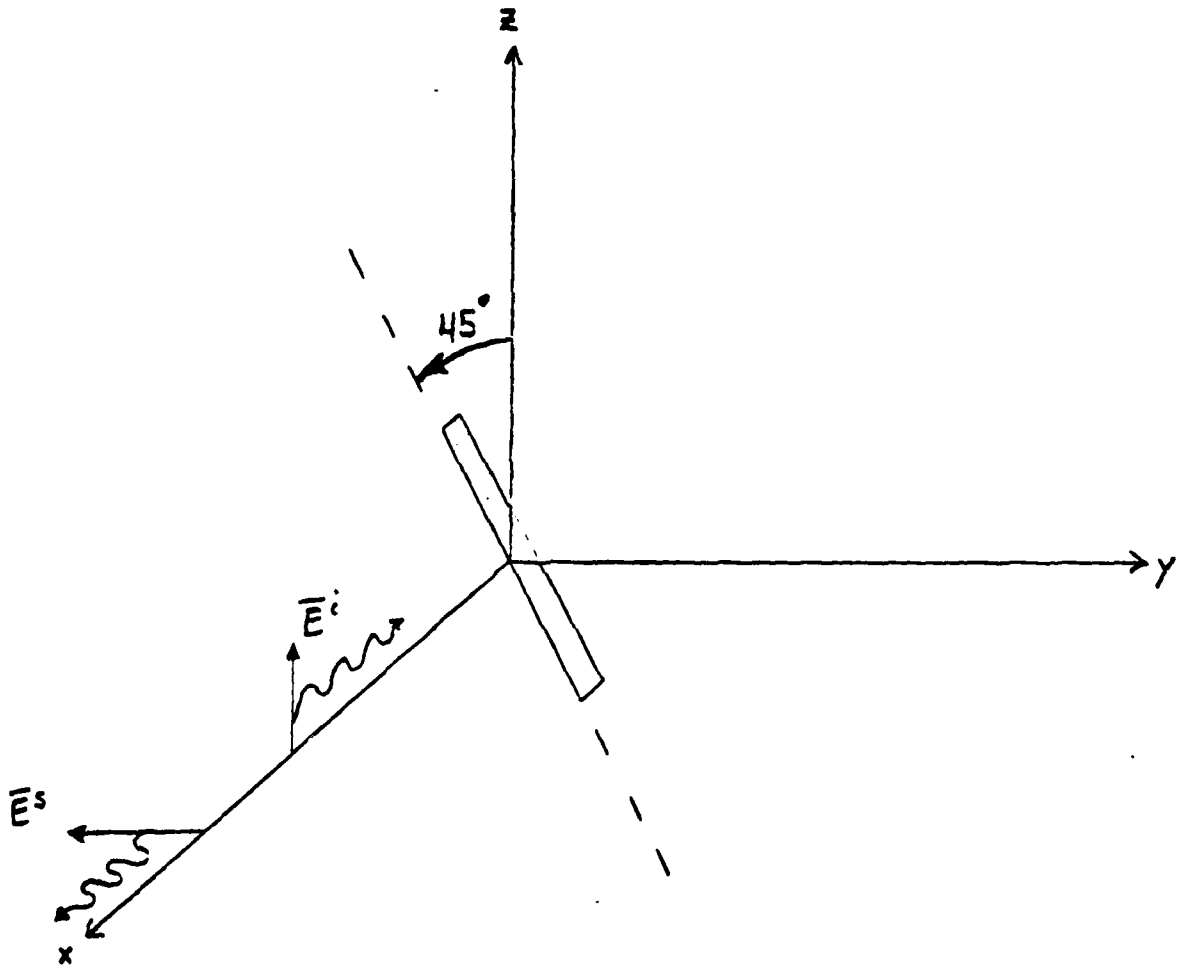

Figure 5-1. Calibration target for cross polarized measurements.

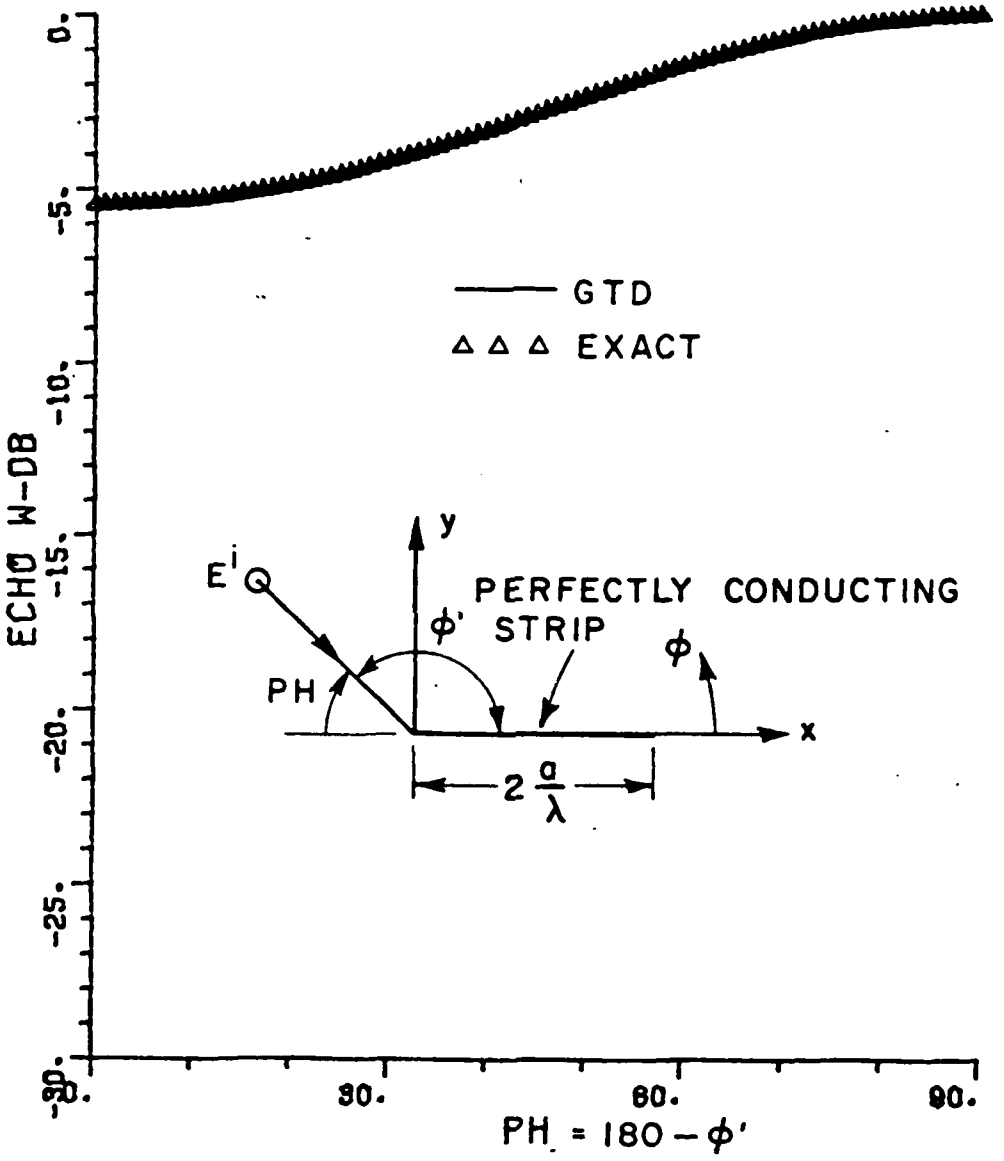

Figure 5-2. H-plane echo width pattern of λ/4 wide strip.

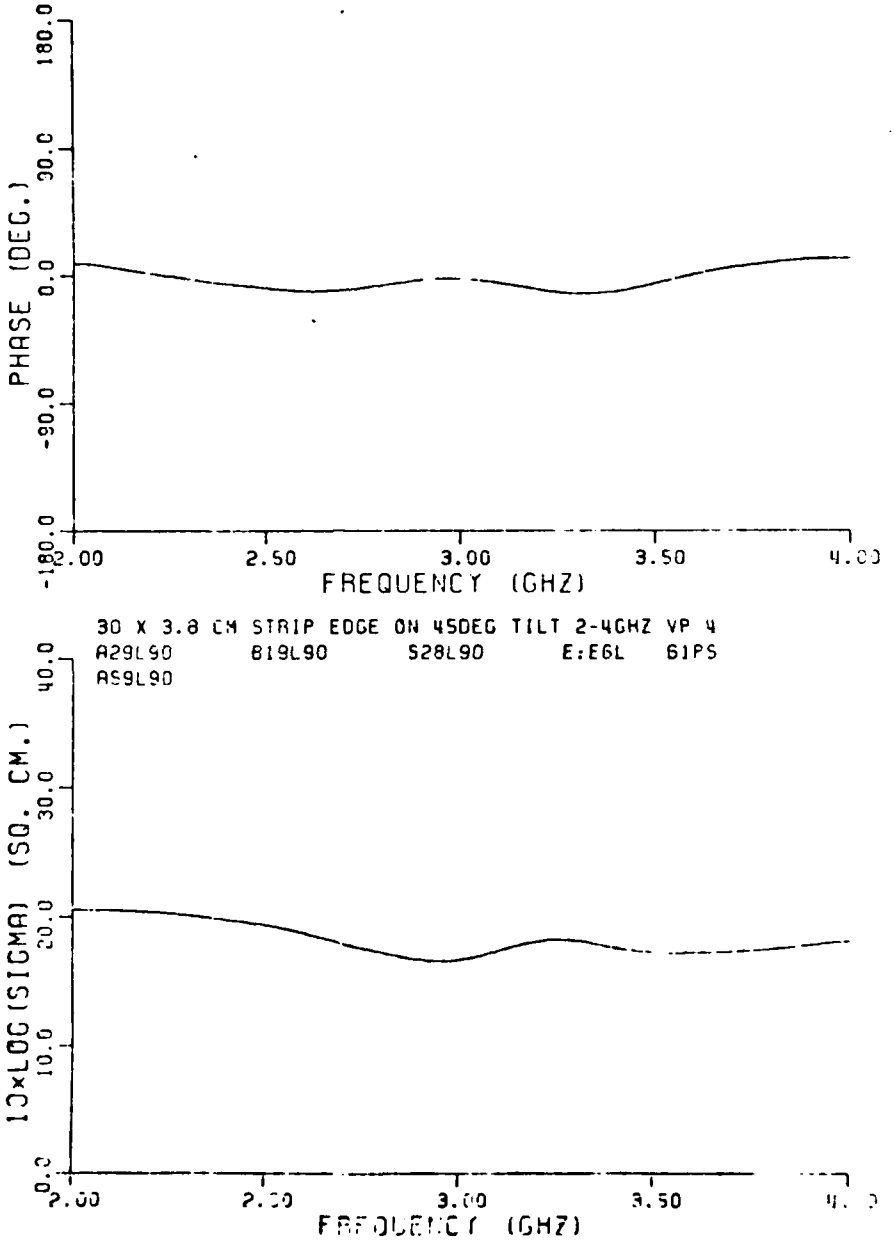

Figure 5-3. Co-polarized measurements of a narrow strip calibrated against a sphere.

The targets described in Chapter II were tilted out of the principal planes in order to ensure a cross-polarized return. In addition to these targets, several sizes of discs, flat plates and strips were included. To test the viability of obtaining cross-polarized results using the strip, the measured spectra were compared to the few existing cross-polarized solutions. In Figure 5-4 an exact solution by D. Hodge [22] is compared to measured cross-polarized results for a disc at edge-on incidence and at a 45° tilt. The results compare very well for those portion of the spectrum above the noise floor of the system. While the cross-polarized target cross section tends to be lower than in the co-polarized case, the noise floor is generally lower for the cross-polarized measurements due to the decoupling of the transmit and receive antennas. The cross-polarized measurements show a reasonable degree of accuracy down to cross sections of 1 sq. cm.

While the time domain analysis is not yet complete, these results demonstrate that the measurement system described in Chapter II has been successfully modified to measure cross-polarizced radar cross sections. The edge-on strip has been shown to be an accurate calibration target, and has been used to obtain the cross-polarized impulse responses given in [23]. The cross-polarization data complete the polarization scattering matrix, and in conjunction with the co-polarized impulse responses, completely characterized the scattering behavior of the targets in question.

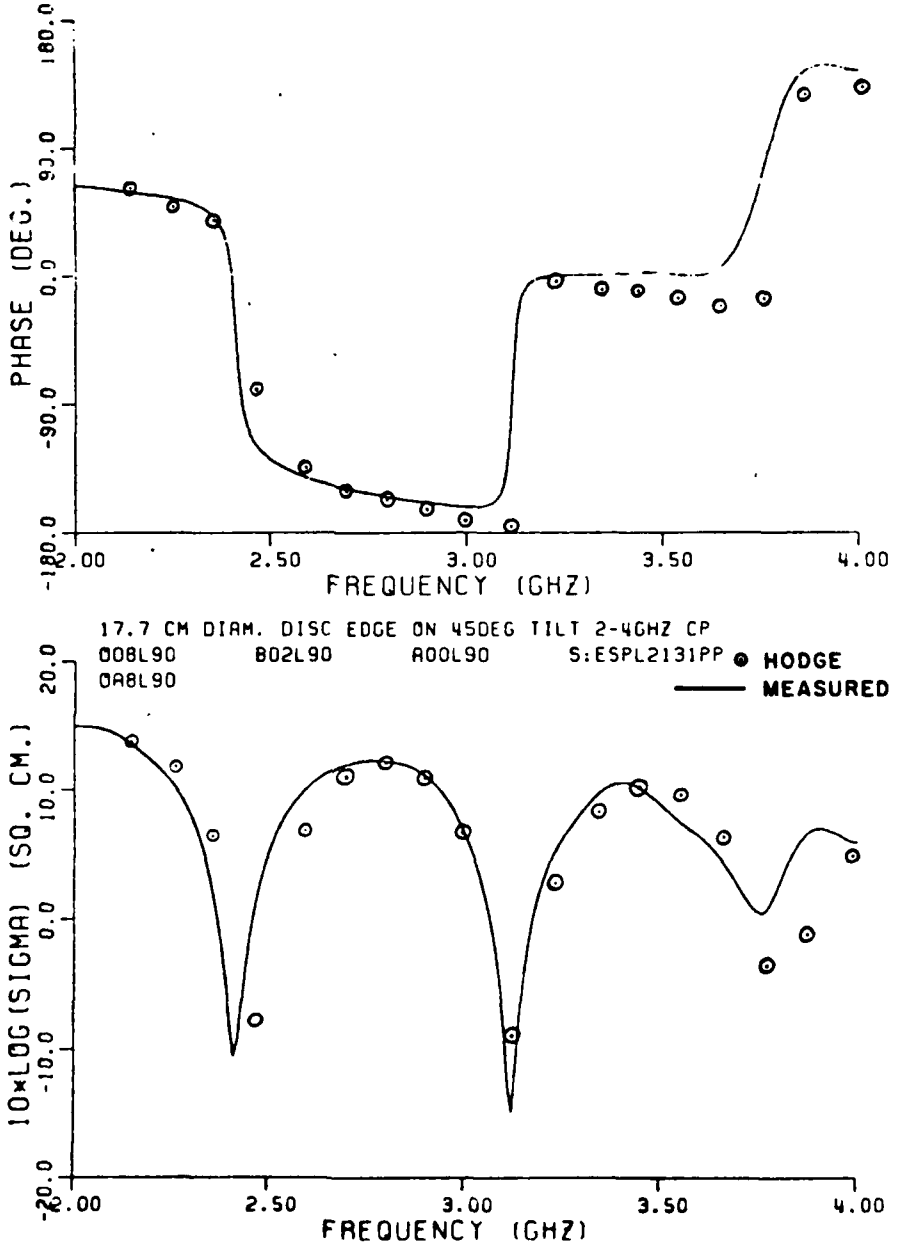

Figure 5-4. Comparison of measured and theoretical (Hodge) cross-polarized response from a thin disk tilted at 45°.

CHAPTER VI

CONCLUSIONS

The impulse response has been shown to offer a physically intuitive view of some relatively complex scattering phenomena. The waveforms presented in Chapter IV are the most accurate measured impulse responses available to date. As a first look, it is only natural that they present more questions than answers. But the intimate relation between the transient waveform and the scattering geometry directs further research toward specific scattering mechanisms. In keeping with the straightforward nature of the impulse response, the scattering analysis has been approached from an intuitive point of view.

We have seen that the early time behavior of the impulse response waveform shows a clear and predictable connection to surface curvature at the specular point. For those aspects at which the scatterer has a reflected field the specular impulse is insensitive to the polarization of the incident field. This is consistent with physical optics. But the return for times immediately following the specular impulse is polarization dependent. The relation between polarization, surface curvatures in the principal planes, and the impulse response waveform

has been discussed for specific examples. For those aspects at which there is no reflected field the initial response is quite sensitive to polarization.

The late time behavior has displayed some characteristic low frequency resonant behavior in a variety of forms. The measured waveforms may support efforts to extract natural poles by analytical methods for the purpose of target identification [25]. The measurements show that not only low frequency transients appear in the late time, but also high frequency multiple diffraction and creeping wave mechanisms.

Finally, by displaying several type of time dispersion, the measured waveforms suggest ways of extending the Uniform Theory of Diffraction solution to account for lower frequency phase dispersion associated with caustic regions.

APPENDIX A

UTD AND PHYSICAL OPTICS APPROXIMATIONS

The physical optics approximation to the impulse response of a scatterer is derived in [4] as,

$$F_I(t) = -\frac{1}{4\pi}\frac{d^2A(Z)}{dZ^2} \quad , Z = \frac{ct}{2} \quad . \tag{A.1}$$

where A(Z) is the cross sectional area intercepted by a plane at Z parallel to the xy plane and moving in the positive Z direction at a speed $c/2$. The form of A(Z) and its second derivative is shown in Figure A-1 for the sphere, Figure A-2 for the 2:1 right circular cylinder at broadside, and Figure A-3 for the disc of radius a.

For the broadside cylinder in Figure A-2 the delta function at Z=0 is not well defined. While the shape of this curve is accurate the proper weight of the impulse would require a limiting procedure for the cylinder slightly off broadside as is done in the UTD expression of Equation (4.13). The behavior near $Z \to 0^+$ varies as $\left(\frac{a}{Z}\right)^{3/2}$ indicating an ill-defined Laplace transform.

In Figure A-3 $\frac{d^2\lambda(Z)}{dZ^2}$ for the disc has the form of a shifted tangent curve. In the limit as $\theta \to \pi/2$ the curve approaches a doublet.

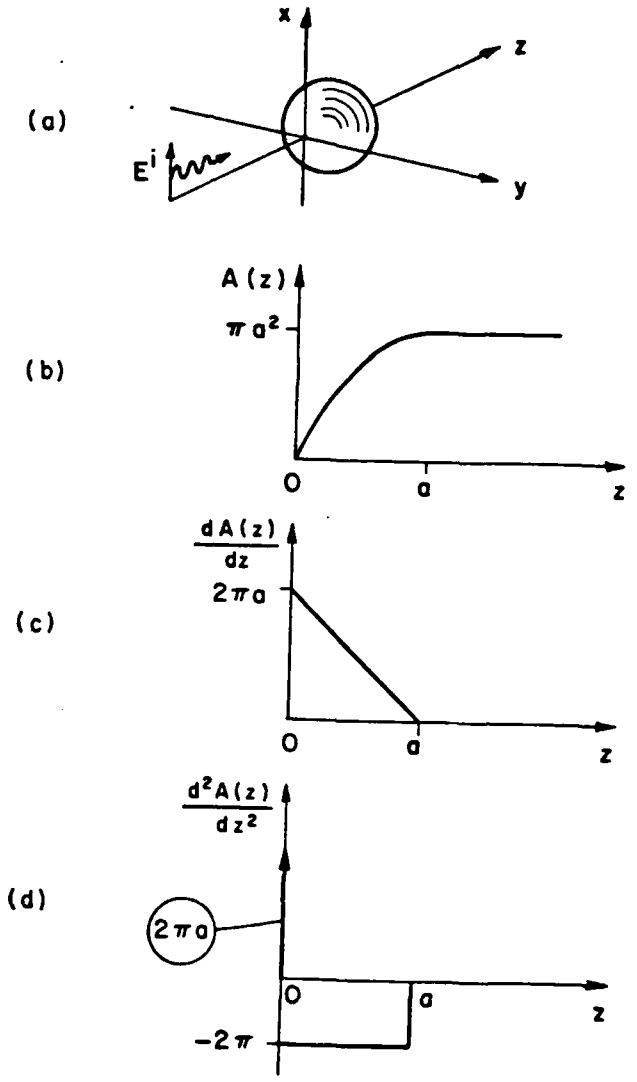

Figure A-1. Cross sectional area function, A(Z), for a sphere or radius a.

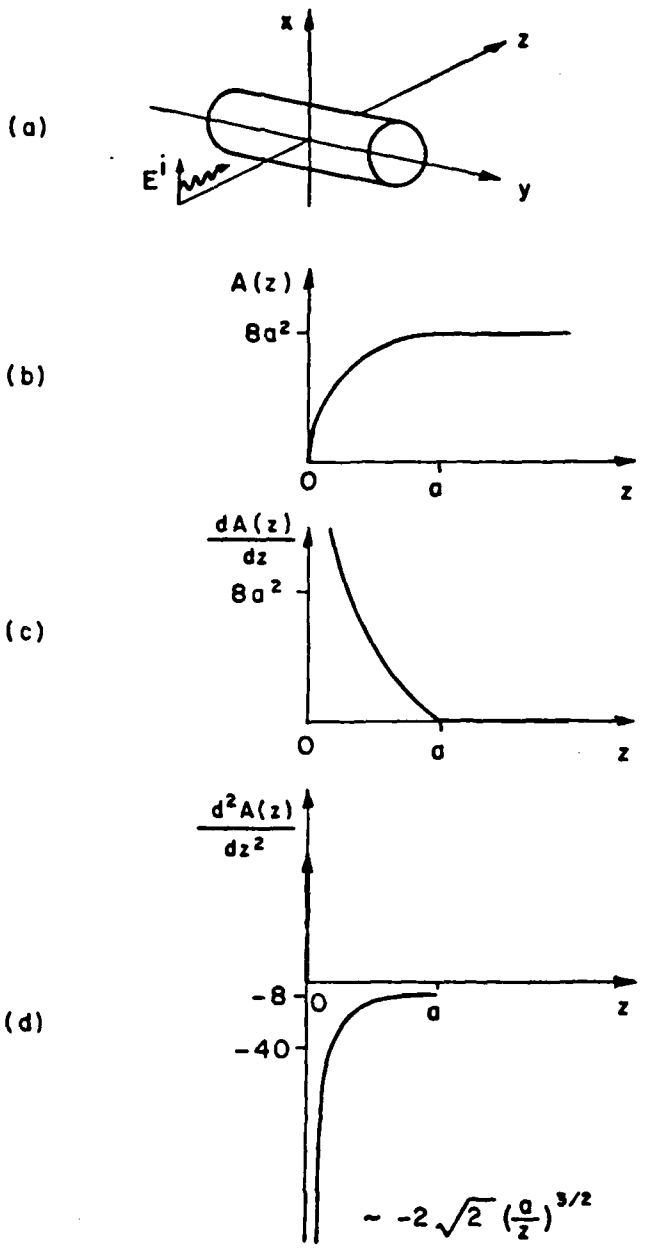

Figure A-2. Cross sectional area function, A(Z), for broadside illumination of a right circular cylinder of diameter 2c and length 4a.

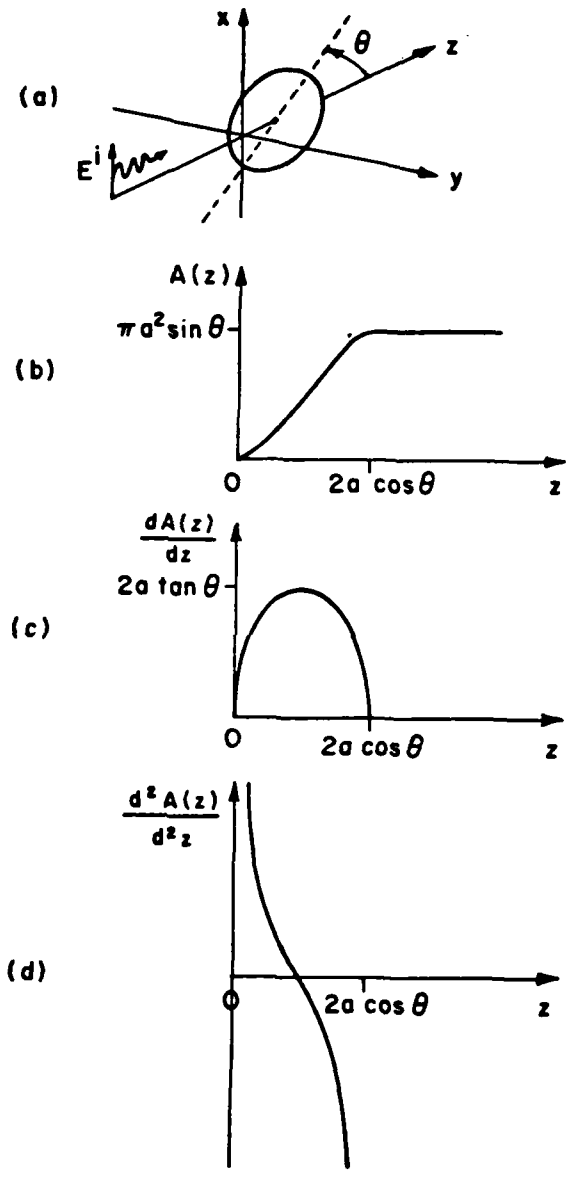

Figure A-3. Cross sectional area function, A(Z), for a disc of radius a tilted away from the Z axis by an angle θ and centered at Z = a cos θ.

The first order UTD solution for the sphere-capped cylinder is well documented in T.T. Chu's dissertation [12]. A sketch of the scattering geometry is given in Figure A-4. For $0 < \phi < 90°$, there is a reflected field from the sphere, a diffraction from the discontinuity in surface, curvature at the junction between sphere and cylinder, and a diffraction from the rear edge. For $90 < \phi < 180°$, there is diffraction from two stationary points on the end of the cylinder and a diffraction from the sphere-cylinder junction.

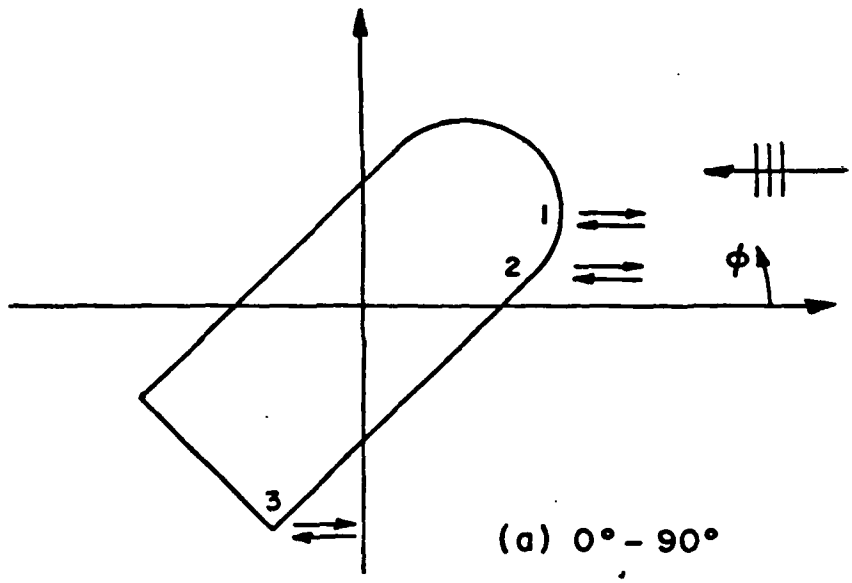

(a) 0° - 90°

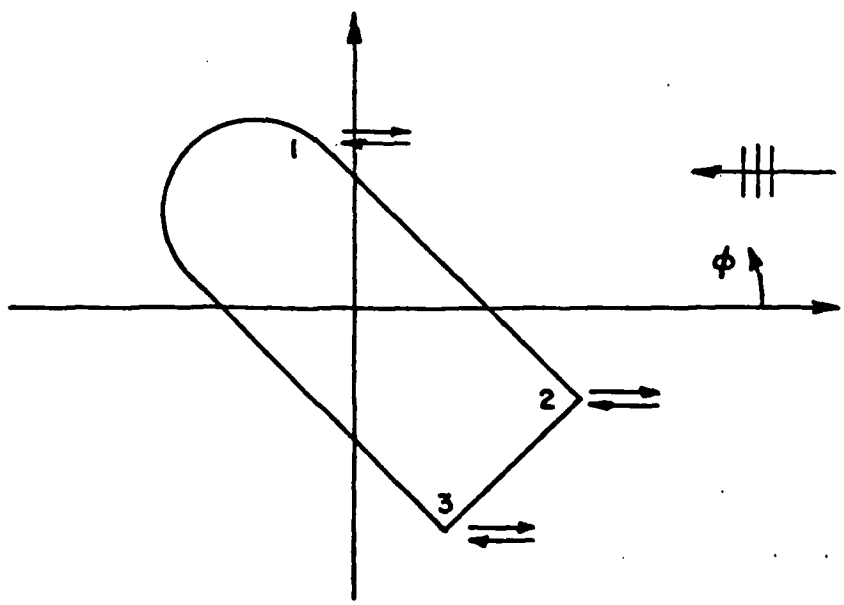

(b) 90° - 180°

Figure A-4. The geometry for the three-point UTD solution.

REFERENCES

[1] Kennaugh, E.M. and R.L. Cosgriff, "The Use of Impulse Response in Electromagnetic Scattering Problems", 1958 IRE National Conv. Rec., pt. 1, pp. 72-77, 1958.

[2] Kennaugh, E.M., "The Scattering of Short Electromagnetic Pulses by a Conducting Sphere", Proc. IRE (Correspondences), Vol. 49, p. 380, January 1961.

[3] Moffatt, D.L. and E.M. Kennaugh, "The Axial Echo Area of a Perfectly Conducting Prolate Spheriod", IEEE Trans. on Antennas and Propagation, Vol. AP-13, pp. 401-409, May 1965.

[4] Kennaugh, E.M. and D.L. Moffatt, "Transient and Impulse Response Approximations", Proc. IEEE, Vol. 53, No. 8, pp. 893-901, August 1965.

[5] Young, J.D., D.L. Moffatt, and E.M. Kennaugh, "Time-domain Radar Signature Measurement Techniques", Technical Report 2467-3, The Ohio State University ElectroScience Laboratory, Department of Electrical Engineering; prepared under Contract No. F44620-67-C-0095 for Air Force Cambridge Research Laboratories, Bedford, Massachusetts, July 30, 1969.

[6] Young, J.D., "Target Imaging from Multiple-Frequency Radar Returns", Technical Report 2768-6, The Ohio State University ElectroScience Laboratory, Department of Electrical Engineering; prepared under Contract No. AFOSR-69-1710 for the Department of the Air Force, Air Force Office of Scientific Research, Arlington, Virginia, June 1971.

[7] Moffatt, D.L., "Impulse Response Waveforms of a Perfectly Conducting Right Circular Cylinder", Proc. IEEE (Correspondences), Vol. 57, No. 5, pp. 816-817, May 1969.

[8] Bennett, C.L., K.S. Menger, R. Hieronymus, J. DeLorenzo, and D. Anderson, "Space Time Integral Equation Approach for Targets with Edges", Sperry Rand Research Center Interaction Note 234, July 1974.

[9] Burnside, W.D. and L. Peters, Jr., "Axial-Radar Cross Section of Finite Cones by the Equivalent Current Concept with Higher Order Diffraction", Radio Science, pp. 943-948, October 1972.

[10] Johnson, T.W., and D.L. Moffatt, "Electromagnetic Scattering by Open Circular Waveguides", Technical Report 710816-9, The Ohio State University ElectroScience Laboratory, Department of Electrical Engineering; prepared under Contract No. N00014-78-C-0049 for the Department of the Navy, Office of Naval Research, Arlington, Virginia, December 1980.

[11] Harrington, R.F., Field Computation by Moment Methods, Krieger Publishing Co., Malabar, Florida, 1982, pp. 42-45.

[12] Chu, T.T., "First Order Uniform Geometrical Theory of Diffraction Analysis of the Scattering by Smooth Structures", Ph.D. dissertation, Ohio State University, 1983.

[13] Keller, J.B., R.M. Lewis, and B.D. Seckler, "Asymptotic Solutions of some diffraction problems", Comm. Pure Appl. Math., vol. 19, pp. 207-265, 1956.

[14] Hu, Y.Y., "Back-scattering Cross Sections of a Center-loaded Cylindrical Antenna", IRE Trans., vol AP-6, No. 1, pp. 140-148, Jan. 1958.

[15] Harrington, R.F., "Time-Harmonic Electromagnetic Fields", McGraw-Hill, New York, N.Y., 1961, p. 357.

[16] King, R.W.P., "The Theory of Linear Antennas", Harvard University Press, Cambridge, Massachusetts, p. 70, 1956.

[17] Pathak, P.H., W.D. Burnside, and R.J. Marhefka, "A Uniform GTD Analysis of the Diffraction of Electromagnetic Waves by a Smooth Convex Surface", IEEE Trans., Vol. AP-28, No. 5, September 1980.

[18] Weir, W.B., L.A. Robinson, D. Parker, "Broadband Automated Radar Cross Section Measurements", IEEE Trans., Vol. AP-22, No. 6, p. 780, November 1974.

[19] Harris, F.J., "On the Use of Windows for Harmonic Analysis with the Discrete Fourier Transform", Proc. IEEE, Vol. 66, No. 1, p. 51, January 1978.

[20] Leeper, W.J. and J.D. Young, "Identification of Scattering Mechanisms from Measured Impulse Response Signatures of Simple Conducting Objects", presented at the International Symposium of the IEEE AP-S, Houston, Texas, May 1983.

[21] Peters, L., Jr., "Two Dimensional Applications for Bodies with Edges", The Ohio State University ElectroScience Laboratory Short Course Notes, Vol. I.

[22] Hodge, D.B., "The Calculation of Far Field Scattering by a Circular Metallic Disk", Technical Report 710816-2, February 1979, The Ohio sTate University ElectroScience Laboratory, Department of Electrical Engineering; prepared under Contract N00014-78-C-0049 for Department of the Navy, Office of Naval Research, Arlington, Virginia 22217.

[23] Young, J.D. and E.K. Walton, "Response Region Backscattered Signatures from a Conducting Ellipsoid", presented at the International Symposium of the IEEE AP-S, Houston, Texas, May 1983.

[24] Burnside, W.D., and L. Peters, Jr., "Edge Diffracted Caustic Fields", IEEE Trans., Vol. AP-22, No. 4, July 1974, pp. 620-623.

[25] Kennaugh, E.M., "The K-pulse Concept", IEEE Trans., Vol. AP-29, No. 2, pp. 327-331, March 1981.


DATE
ILME